Investigating spectral wave properties and their effects on bottom evolution induced by waves and current

Author:
S.J.M. Boersen
3689735 (UU)
4328086 (TUD)

Supervisors:
prof. dr. H.E. de Swart
prof. dr. ir. A.J.H.M. Reniers
dr. ir. B.C. van Prooijen
dr. ir. M.A. de Schipper
dr. D.S. van Maren
dr. A.S. von der Heydt
S. Meirelles, MSc

January 13, 2017

Utrecht University

TU Delft
Delft University of Technology

Deltares
Enabling Delta Life

Preface

This thesis concludes my double degree programme consisting of a master Meteorology, Physical Oceanography and Climate at Utrecht University and a master Hydraulic Engineering at Delft University of Technology. When I started this program, I did not know what to expect from the combination of both programs and what problems I would run into. I only hoped that my interests in the subjects was larger than the challenges I would phase. It took me exactly 20 days longer than I originally planned, but in the end it all worked out.

Additional to Delft University of Technology and Utrecht University, the researched institute Deltares also participated in this research. I would like to thank my daily supervisors Huib de Swart and Bram van Prooijen for the time they invested in me and their constructive feedback. Furthermore, I would like to thank all the other members of the graduation committee: Ad Reniers, Bas van Maren, Saulo Mereilles, Matthieu de Schipper and Anna von der Heydt.

Also, I would like to thank my family for their understanding and apologize for all the birthdays and other activities I had to cancel the last year. Finally, I would like to thank my fellow students at the universities and at Deltares. Special thanks to Gerben, Felix, Cindy, Tjebbe, Melanie, Brenda and Rufus for their enthusiastic support and their help with the daily struggles.

Stef Boersen
Delft, January 2017

Abstract

In many coastal seas, wind-generated waves produce a strong bottom orbital velocity which stirs up sand from the bottom. This process strongly influence sediment transport and bottom evolution.

State-of-the-art morphodynamic models traditionally represent the stirring of sand by irregular waves in a highly parametric way. For instance, the bottom orbital velocity is computed on the basis of a single representative wave with the peak period as wave period. This traditional approach does not properly account for the often complex distribution of the wave energy in the spectral domain, as revealed by the wave spectrum. The effects of this parametrisation on the bottom orbital velocity and sediment transport are unclear and motivate the current research.

In this study, a new method is applied to compute the amplitude of the bottom orbital velocity, using spectral information. This method considers a sinusoidal wave for each individual frequency and calculates its contribution to the bottom orbital velocity. The impact of the new method was investigated using a point model, field measurements and a numerical morphodynamic model. The point model computes the bottom orbital velocities for a given wave spectrum for both methods. The field measurements are combined with the point model to validate the new method. The numerical morphodynamic model asses the implications on sand transport and the formation of ebb-tidal deltas, i.e., bodies of sand that are located seaward of a tidal inlet.

The point model showed that the bottom orbital velocity using the new method was between 20% lower and 60% higher relative to the traditional method, depending on the peak period and depth. The difference arises from the frequency-dependent reduction of the bottom orbital velocity by depth. The field measurements suggest that the new method reduces the root-mean-square error between the calculated and measured bottom orbital velocity amplitude reduces by 30% compared to the traditional method. The morphodynamic model reveals that applying the spectral method leads to deeper channels and larger shoals. The computational effort of both methods were similar. The new method is recommended if the peak period is small ($\leq\sim$ 6 s), the depth is large ($\geq\sim$ 10 m) and/or if the wave spectrum is wide.

Contents

Chapter 1

Introduction

1.1   Sand transport and bed forms in coastal areas

In coastal seas, for example the North Sea, strong currents and high waves can be observed. The combination of current and waves exerts a force on the sea bed. When this force is large enough and the bed is mobile, sediments are being transported. Spatial variations in sediment transport lead to changes in morphology. The morphological changes give rise to a complex system of bed forms, for example the complex morphology located in the Wadden Sea (see Figure 1.1).

Figure 1.1: Bathymetry of the western Wadden Sea combined with the satellite image of this region using Open Earth Tools. The red and orange line indicate the dikes that close the Zuiderzee and Lauwerzee. The numbers 1 to 4 indicate the Texel Inlet, Vlie Inlet, Ameland Inlet and the Zoutkamperlaag Inlet, respectively. The bathymetry was measured in the period 2006 to 2012 by Rijkswaterstaat. *Reprint from Ridderinkhof [2016]*

Bed forms are important because of their high economical and ecological values. Firstly, several of them are identified as Natura 2000 areas by the European Commission [*Jak et al.*, 2009], for example the ebb-tidal delta (large body of sand located seaward of a tidal inlet) in the Western Scheldt estuary (The Netherlands), indicating their ecological value. Secondly, bed forms can migrate over the bed and therefore be a threat to navigation channels [*Herman et al.*, 2016]. Finally, bed forms are an integrated part of coastal systems and human interventions in bed forms influence the entire system [*deltacommissaris*, 2016]. To investigate the natural behaviour and the effects of human interventions on bed forms morphodynamic models are used. In the past decades, numerical models have contributed to the understanding and the prediction of the coastal systems. However, these models are still based on a number of assumptions that reduce the viability of the outcomes.

1.2 Morphodynamic modelling

The reliability of the outcomes of numerical models depends on a range of assumptions. Roughly, it can be stated that numerical models rely on: (i) representation of the physical mechanisms; (ii) numerical implementation; (iii) initial conditions and boundary conditions. Considering the simulation of coastal areas, improvements can be made on all these aspects. In this thesis, we consider an aspect that belongs to the first category: physical representation of the mechanisms. In particular on the wave induced velocity on the bed.

Different models have a different representation of the same physical mechanism. Important is this study is the physical representation of wave. Two distinctions can be made: a phase averaged description, for example used in Delft3D [*Lesser et al.*, 2004] or a phase resolving representation, for example applied in SWASH [*Zijlema et al.*, 2011]. A phase averaged model only considers the effect of the wave, averaged over a wave period. On the other hand, a phase resolving model integrates the intra-wave processes as well. The advantage of a phase averaged model it is computational effort. It is low enough for large scale morphodynamic modelling.

In phase averaged models, the physical processes which lead to a morphological change are modelled in a highly parametric way. The forces by the current and waves on the bed are calculated separately and combined to determine the total force [*Soulsby et al.*, 1993]. The forces by the current are determined on the current velocity and a roughness coefficient. Similarly, the forces by waves are resolved using the amplitude of the bottom orbital velocity (u_b), the wave induced velocity at the bottom and a friction factor.

Problems arise when irregular waves are considered instead of monochromatic waves. To determine the forces by waves on the bed for irregular waves an equivalent (monochromatic) wave needs to be determined. The value of u_b is calculated for this equivalent wave. The classical equivalent wave is based on bulk wave parameters, such as the root-mean-square wave height (H_{rms}) and peak period (T_p) and neglects the distribution of the wave energy over the different frequencies. This method is referred to as the bulk method.

Other equivalent wave concepts have been formulated and some of them take into account the distribution of wave energy over the different frequencies. One of them is the formulation by *Soulsby and Smallman* [1986], also explained in *Soulsby* [1987] and *Soulsby* [1997]. This method, hereinafter referred to as the spectral method, calculates the contribution of each wave in the value of u_b individually. The spectral method was validated by *Ockenden and Soulsby* [1994]. More recently *Wiberg and Sherwood* [2008] validated the method of *Soulsby and Smallman* [1986] in deeper waters and *Yuan* [2016] applied the same EWC in an oscillatory water tunnel.

1.3 Problem statement and research questions

Considering the previous research and the importance of morphodynamic modelling, the aim of this study is to implement the spectral method into a complex numerical model and to investigate the effects of considering the wave spectrum on the bottom evolution. This research will also determine if large errors arise when the wave energy distribution is neglected. The validation of the spectral method was limited to deep water. Because morphodynamic models are also used in shallow water additional validation is required.

As a result, the following research questions are defined:
1. How do the water depth, root-mean-square wave height, peak period and spectral shape influence the difference between a bottom orbital velocity amplitude calculated using the bulk method and the spectral method?
2. Is the calculated bottom orbital velocity amplitude significantly improved when a spectral

method is used instead of a bulk method?

3. How does the spectral method used to compute the bottom orbital velocity amplitude and subsequent sediment transport influence the modelled morphodynamic behaviour of complex systems compared to the situation when the bulk method applied?

1.4 Approach

To answer the three research questions, approaches specifically for each question are used (see Figure 1.2). To answer the first research question (RQ 1) a point model is developed. This point model solely determines the values of u_b using the formulations of *Soulsby and Smallman* [1986] and the bulk method for different values of h, T_p, H_{rms} and different spectral shapes. Effects of current or bed level change are not considered.

For the second research question (RQ 2) field data is combined with the point model to determine a u_b value by the bulk and the spectral method. These values are compared with a value of u_b based on a velocity measurement at the bed. For the bulk and the spectral method a time series of the surface elevation is applied.

Two Delft3D schematisations are involved for the third research question (RQ 3). Delft3D is chosen because the computational effort is small enough to model complex morphological systems. The spectral method is implemented in Delft3D. As complex system, a ebb-tidal delta is investigated. In these systems both waves and current are important and their is a large depth variations. The first schematisation of an ebb-tidal delta is based on the Vlakte van de Raan located in the Western Scheldt estuary. This simulation will show the effect of accounting for the spectral method in a realistic complex geometry. The spectral method is further tested by determination the effects on the morphological response. To focus on the morphological behaviour, an idealised sechematisation is used.

1.5 Outline

The next chapter will start with a brief introduction into sediment transport. This is followed by the mathematical formulation of the spectral and bulk method. Finally, an explanation of the equations used in Delft3D are given. Chapter 3 explains the measurements and extraction of the wave induced time signals. In this chapter the two Delft3D schematisations and model settings as well as the their parameters and settings are also discussed. Furthermore, this chapter will contain the settings of the point model. The results are presented and explained in Chapter 4. Some remarkable aspects of the results, as well as several limitations and recommendations for further research are given in Chapter 5. This thesis ends with the conclusions in Chapter 6 which provides answers to the three research questions.
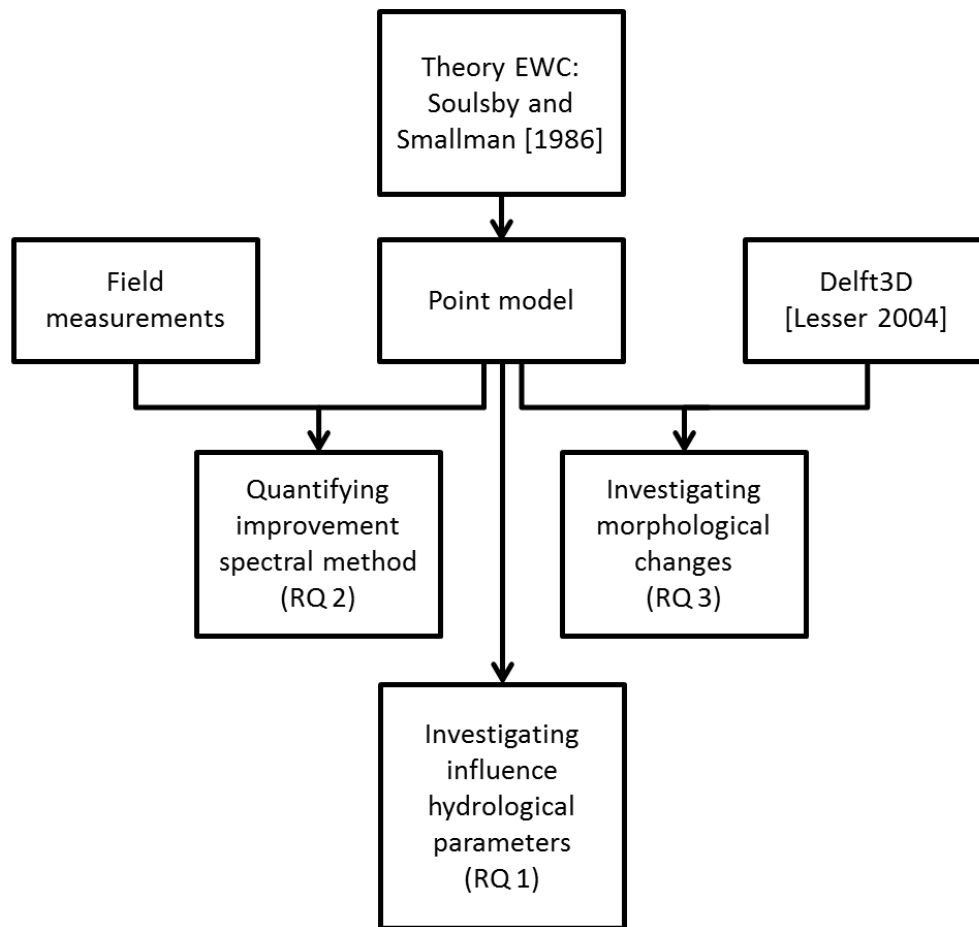
EcoShape [2016]

Figure 1.2: A schematic overview of the approach used in this study, with RQ as Research Question.

Chapter 2
Theoretical concepts

This chapter describes the theoretical concepts that will form the backbone of this thesis. First, an introduction into sediment transport is given. After that, Section 2.2 concentrates on the formulations to calculate the bottom orbital velocity for the spectral and bulk method. Section 2.3 gives a description of the point model and its mathematical formulations. This model is used to investigate the effect of water depth, root-mean-square wave height, peak period and spectral shape on the difference between a bottom orbital velocity amplitude calculated using the bulk method and the spectral method. In this part, current and bed level changes are not considered. Finally, Section 2.4 explains the Delft3D formulations. Delft3D will be used for the complex numerical modelling.

2.1 Introduction to sediment transport

There are different types of sediment transport: bedload, suspended load and wash load transport (see Figure 2.1). For bedload transport, the sediments are transported over the bed by saltating, sliding and rolling. In case of suspended load transport the sediments are in suspension and no longer in contact with the bed. The wash load transport is the transport of relative very fine sediment. Its effects on the bathymetry are often neglected because the deposition of these sediments is minimal. Furthermore, it can be stated that they are always in suspension.
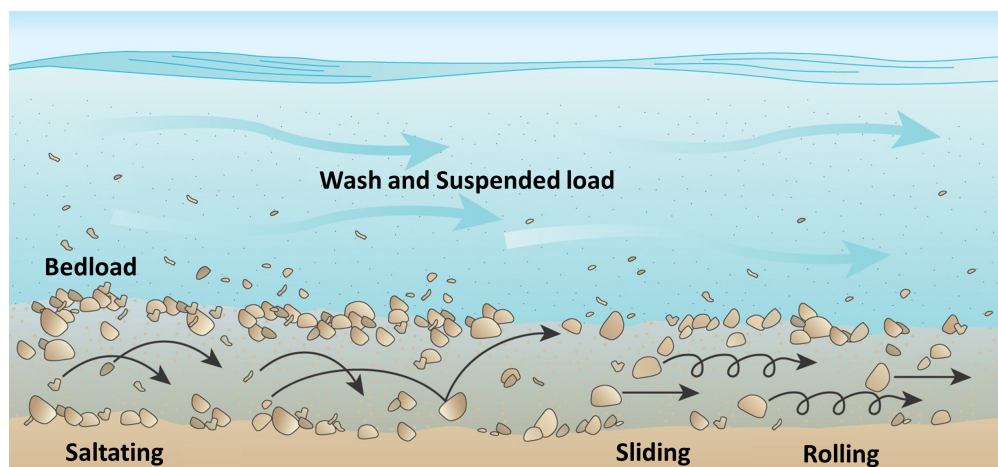

Figure 2.1: A graphical representation of the different types of sediment transport: bedload, suspended load and wash load (dissolved load) transport *Adapted from Paerson Prentice Hall Website.*

Sediments are being transported if the driving forces are larger than the resisting forces and these forces determine the type of sediment transport. For instance, in case of a large boulder the suspend transport can be neglected because the driving forces are not able to bring this boulder into suspension. For very fine sand the resisting forces are very small and the sand can be brought into suspension more easily. In this study non-cohesive sand is investigated and because of that the bedload and suspended load transport are taken into account.

Two important driving forces of sediment transport are waves and current. They both induce a

shear stress on the bed, the bed shear stress. An important difference between the current induced bed shear stress and the wave induced bed shear stress is their variation in time. The flow induced bed shear stress is constant in time if the flow conditions are stationary. On the other hand, if the wave conditions are constant in time than the wave induced bed shear stress still changes with the wave period. Furthermore, the direction of the wave induced bed shear stress changes during a wave cycle and as a result, the net sediment transport purely by waves is much smaller than the instantaneous transport. Therefore, in case of sediment transport due to waves and current it is often interpreted that wave stir up the sediment, while the current transports it.

Although sediments are transported, it does not mean that the bathymetry alters. A change of the sediment transport in the horizontal direction leads to a change in the bathymetry. When the sediment transport increases/decreases, the bathymetry erodes/accumulates.

The initiation of motion is difficult to determine due to the shape and the roughness of the individual sediment grains and because of that a critical Shields parameter (θ_{cr}) is often used [*Shields*, 1936]. This parameter represents the drivering versus the resisting forces. In this study, it calculated using the formulation of *Soulsby and Whitehouse* [1997] because the transport of sand by waves and current is investigated:

$$\theta_{cr} = \frac{0.24}{D_*} + 0.55 \left(1 - e^{-0.02D_*}\right) \tag{2.1}$$

with D_* the dimensionless grain size given by

$$D_* = \left[\frac{g(\rho_s/\rho - 1)}{\nu}\right]^{1/3} \tag{2.2}$$

with g as the gravitational acceleration, ρ_s as the density of the sediment grains, ρ as the density of the fluid and ν the kinematic viscosity of water. The value of θ_{cr} is converted into a critical bed shear stress, τ_{cr},

$$\tau_{cr} = \theta_{cr} \left(\rho_s - \rho\right) gD \tag{2.3}$$

with D the sediment grain size. This can be interpreted as the minimum required stress to initiate the motion of sediments. Equation 2.3 shows that if the grains are larger or have a higher density, it is more difficult to transport them.

Sediment transport is much more complicated than is explained in this introduction. First of all, the bed shear stress by waves and current is very complicated because the combined bed shear stress is larger than the linear summation of the wave-alone and current-alone stress [*Soulsby et al.*, 1993]. Furthermore, for the effects of bottom slope one is referred to *Van Rijn* [1993].

2.2   Equivalent wave concept

The equivalent wave concept of *Soulsby* [1987] is applied in this study. This concept approximates a wave signal by a summation of linearly independent waves with random phase. For each wave the bottom orbital velocity is calculated and summed for the entire spectrum of wave, i.e.

$$u_b^2 = \int_0^\infty \frac{2\omega^2 \tilde{E}}{\sinh^2(kh)} d\omega \tag{2.4}$$

with ω as the angular frequency, $\tilde{E}$ is the wave energy density, k is the wave number and h is the local water depth. In the frequency domain this relation can be interpreted as a transformation of

the wave energy density spectrum into a bottom orbital velocity variance spectrum follow by an integration of velocity spectrum. On the other hand, in the time domain it can be explained as a wave signal which is divided into linear independent waves with each its own amplitude. Each wave results in a value of u_b and these values are added. This spectral method will be compared with a bulk method which is based on the current formulation used in Delft3D

$$u_b^2 = \frac{2\omega_p^2 \int_0^\infty \tilde{E} d\omega}{\sinh^2(k_p h)} \tag{2.5}$$

with u_b the bottom orbital velocity amplitude, ω_p as the peak angular frequency ($\omega_p = 2\pi/T_p$) and k_p is the peak wave number based on ω_p. Equation 2.5 does not contain the physical process that waves with a larger wavelength penetrate deeper into the water than wave with a shorter wavelength. This process is taken into account when Equation 2.4 is used. The values of u_b are equal for both equations when the shape of the wave spectrum is narrow.

2.3 Point model

The point model converts bulk wave statistics into a wave spectrum and calculates u_b using the spectral method and the bulk method. Different types of spectral shapes can be described by a similar relation:

$$\tilde{E} = \frac{\chi H_{rms}^2}{8} \frac{f_p^4}{f^5} \exp\left[-\frac{5}{4}\left(\frac{f}{f_p}\right)^{-4}\right] \gamma^{\phi(f/f_p)} \tag{2.6}$$

$$\text{with } \phi(f/f_p) = \exp\left[-\frac{1}{2\xi^2}\left(\frac{f}{f_p} - 1\right)^2\right]$$

Here, H_{rms} is the root-mean-square wave height, f_p is the peak frequency and f is the frequency. The shape of the spectrum is determined by χ, γ and ξ [*Chakrabarti*, 1986]. The spectrum is discretised per frequency band, $\tilde{E}_i = \tilde{E}(f_i)$ with $f_i = f_L + \Delta f(i - \frac{1}{2})$. Here, Δf is the width of a frequency band, given by $(f_L - f_R)/N = \Delta f$ with f_L and f_R as the left and right cut-off frequency of the energy density spectrum and N the number of frequency bands.

The spectrum is converted into $\tilde{u}_{b,i}^2$, a discretized bottom orbital velocity variance density spectrum, using linear wave theory [*Mei et al.*, 2005] by

$$\tilde{u}_{b,i}^2 = \left(\frac{2\pi\sqrt{2}f_i}{\sinh(k_i h)}\right)^2 \tilde{E}_i \tag{2.7}$$

with k_i as the wave number for the frequency band i. The value of k_i is determined by solving the dispersion relation individually for each frequency band,

$$\omega_i^2 = gk_i \tanh(k_i h) \tag{2.8}$$

with ω_i as the angular frequency of a frequency band ($\omega_i = 2\pi f_i$). The value of u_b using the spectral method ($u_{b,s}$) is determined by a summation of the velocity variance spectrum, i.e,

$$u_{b,s} = \left(\sum_{i=1}^N \tilde{u}_{b,i}^2 \Delta f\right)^{\frac{1}{2}} \tag{2.9}$$

In the bulk method the shape of $\tilde{E}$ is neglected by summation of the discretized energy spectrum, i.e.,

$$H_{rms}^2 = 8 \sum_{i=1}^{N} \tilde{E}(f_i) \Delta f \tag{2.10}$$

The value of u_b is calculated by

$$u_{b,b} = \frac{\pi f_p H_{rms}}{\sinh(k_p h)} \tag{2.11}$$

with $u_{b,b}$ the bottom orbital velocity determined by the bulk method. The value of k_p is, similar to the spectral method, determined by the dispersion relation

$$\omega_p^2 = g k_p \tanh(k_p h) \tag{2.12}$$

2.4 Delft3D

Two complex systems will be studied by Delft3D. Delft3D is a numerical hydrodynamical and morphological model which consists of several modules. In this thesis the flow module (as discussed by *Lesser et al.* [2004]) is combined with the wave module (described by *Holthuijsen* [2007]). Slight changes of the Delft3D source code were required for this research. For the comparison with the default source code in Delft3D and the code used in this study one is referred to Appendix B.

2.4.1 Flow

The flow module of Delft3D numerically solves the depth integrated shallow water equations in its 2D horizontal configuration, i.e.,

$$\frac{\partial h}{\partial t} + \frac{\partial (hu)}{\partial x} + \frac{\partial (hv)}{\partial y} = 0 \tag{2.13}$$

$$\frac{\partial u}{\partial t} + u\frac{\partial u}{\partial x} + v\frac{\partial u}{\partial y} - fv = -g\frac{\partial \eta}{\partial x} - \frac{\tau_x}{\rho h} + \tag{2.14}$$

$$+ \frac{1}{h}\left[\frac{\partial}{\partial x}\left(\nu_e h\frac{\partial u}{\partial x}\right) + \frac{\partial}{\partial y}\left(\nu_e h\frac{\partial u}{\partial y}\right)\right] + \frac{F_x}{\rho h}$$

$$\frac{\partial v}{\partial t} + u\frac{\partial v}{\partial x} + v\frac{\partial v}{\partial y} + fu = -g\frac{\partial \eta}{\partial x} - \frac{\tau_y}{\rho h} + \tag{2.15}$$

$$+ \frac{1}{h}\left[\frac{\partial}{\partial x}\left(\nu_e h\frac{\partial v}{\partial x}\right) + \frac{\partial}{\partial y}\left(\nu_e h\frac{\partial v}{\partial y}\right)\right] + \frac{F_y}{\rho h}$$

Here, t is time, x and y are the horizontal dimension in longitudinal and latitudinal direction, u and v are the depth averaged velocities in x and y-direction, f is the Coriolis parameter, η is the sea surface elevation with respect to the undisturbed water level, τ_x and τ_y are the combined wave and current induced bed shear stress in x and y-direction, ν_e is the horizontal eddy viscosity. The value of η is related to the change in surface due to long wave, for example tidal elevation. The wave induced forces F_x and F_y are given by the minus divergence of the radiation stress tensor $\overline{\overline{S}}$ [*Longuet-Higgins and Stewart*, 1962],

$$F_x = -\frac{\partial S_{xx}}{\partial x} - \frac{\partial S_{xy}}{\partial y} \qquad\qquad F_y = -\frac{\partial S_{yx}}{\partial x} - \frac{\partial S_{yy}}{\partial y} \tag{2.16}$$

with S_{xx} and S_{yy} the diagonal elements of $\overline{\overline{S}}$ and S_{xy} the non-diagonal elements of $\overline{\overline{S}}$.

2.4.2 Wave

The wave module of Delft3D uses the wave action model SWAN [*Holthuijsen*, 2007]. Wave action density ($\tilde{N}$) is defined as

$$\tilde{N} \equiv \frac{\tilde{E}}{\sigma} \tag{2.17}$$

with σ as the relative frequency given by

$$\sigma = 2\pi f - \vec{k} \cdot \vec{u} \tag{2.18}$$

with $\vec{k}$ as the wave vector and $\vec{u}$ is the velocity vector of the current. SWAN solves the wave action density balance science this a conserved quantity [*Crapper*, 1985]. The balance reads

$$\frac{\partial \tilde{N}}{\partial t} + \frac{\partial c_{g,x} \tilde{N}}{\partial x} + \frac{\partial c_{g,y} \tilde{N}}{\partial y} + \frac{\partial c_\theta \tilde{N}}{\partial \theta} + \frac{\partial c_\sigma \tilde{N}}{\partial \sigma} = \frac{S}{\sigma} \tag{2.19}$$

with $c_{g,x}$ and $c_{g,y}$ as the group velocity in x and y-direction, θ is the spectral direction, c_θ and c_σ are the propagation velocity in spectral space. The sources and sinks of $\tilde{N}$ are represented by S. The second and third term of Equation 2.19 describe the propagation of wave action over the domain. Furthermore, the fourth term models wave refraction and the fifth term describes the shifting of the relative frequency due to variations in current and depth.

2.4.3 Sediment transport

In this study both the bedload and suspended load are considered using *van Rijn* [2007a] and *van Rijn* [2007b]. The suspended sediment is modelled by a depth averaged advection-diffusion equation:

$$\frac{\partial (hc)}{\partial t} + \frac{\partial (huc)}{\partial x} + \frac{\partial (hvc)}{\partial y} + \tag{2.20}$$

$$- \frac{\partial}{\partial x} \left(hD_H \frac{\partial c}{\partial x} \right) - \frac{\partial}{\partial y} \left(hD_H \frac{\partial c}{\partial y} \right) = \frac{w_s(c_{eq} - c)}{T_{sd}} \tag{2.21}$$

Here, c indicates the depth- and wave-averaged sediment concentration, D_H the horizontal eddy diffusion coefficient, w_s the settling velocity and T_{sd} a empirical parameter that depends on the settling velocity. The change is bed level is determined by

$$\frac{\partial z_b}{\partial t} = -\frac{1}{1-p} \left(\frac{\partial q_{b,x}}{\partial x} + \frac{\partial q_{b,y}}{\partial y} + \frac{w_s(c_{eq} - c)}{T_{sd}} \right) \tag{2.22}$$

with $q_{b,x}$ and $q_{b,y}$ the bedload transport in x and y-direction.

Summary: This chapter has described the theoretical concepts which form the background of this thesis. An introduction into sediment transport was given. Additionally, the EWC was explained. The point model was described along with characterisation of Delft3D. The next chapter will describe the different spectra used in the point model. Furthermore, the measurements and Delft3D schematisations will be discussed.

Chapter 3
Materials and methods

In this chapter the methodology and material applied to answer the three research questions is clarified. As was indicated in the Introduction, a different approach is applied for each research question. The formulations used by these different approaches have already been explained in Chapter 2. Here, the exact values of the parameters in the formulations are given. This chapter starts by defining the parameters of the point model. The point model, defined in Section 2.3 and used for the first research question, determines the bottom orbital velocity amplitude (u_b) for the bulk as well as for the spectral method. The parameters determine the hydrodynamic conditions as well as the shape of the wave spectrum. Three deep water wave spectra will be investigated. Section 3.2 explains the field data which is used to quantify the improvement in physical agreement of the calculated u_b by the spectral method. The field data consist of a surface elevation measurement and a velocity measurement at the bottom. Due to their high measuring frequency (> 1 Hz) of both time signals the quantification is possible. This section also explains the filtering procedure to extract the wave induced parts from the measured signals. In Section 3.3 and 3.4 the schematisations and boundary conditions of two Delft3D simulations is explained. In Section 3.3 a complex geometry is considered. On the other hand, Section 3.4 explains a more idealised schematisation. Here, morphological changes are considered. Both schematisations are used to investigate the influence of the spectral method on the modelled morphodynamic behaviour of ebb-tidal deltas compared to the bulk method.

3.1 Point model

In the point model three different spectra will be investigated: The One-Parameter Pierson-Moskowitz spectrum, the Bretschneider spectrum and the JONSWAP spectrum (see Table 3.1). The One-Parameter Pierson-Moskowitz spectrum is, as the name suggests, an one parameter spectrum and is only depending on the peak period (T_p). The JONSWAP and the Bretschneider spectrum are also dependent on the root-mean-square wave height (H_{rms}). In case of the One-Parameter Pierson-Moskowitz spectrum the value H_{rms} is related to the value of T_p by an empirical relation: $H_{rms} = 0.0283T_p^2$ [*Journée and Massie*, 2000]. The three spectra are all deep water spectra and consequently not valid in shallow water. This limitation is further discussed in Section 5.1.

Spectral shape \ Parameter	χ	γ	σ
One-Parameter Pierson-Moskowitz [*Pierson and Moskowitz*, 1964]	5	1	n/a
Bretschneider [*Bretschneider*, 1963]	5	1	n/a
JONSWAP [*Hasselmann et al.*, 1973]	3.29	3.3	0.07, $f < f_p$ 0.09, $f \geq f_p$

Table 3.1: The coefficients to define the three spectra available in the point model. In combination with Equation 2.6 the wave energy density is constructed.

The hydrodynamic conditions, except the type of wave spectrum, are given in Table 3.2. The

value of T_p is set to 8 s, which is a typical value for wind-generated waves [*Holthuijsen*, 2007]. For the Pierson-Moskowitz spectrum this results in a H_{rms} of 1.80 m and because of that the value of H_{rms} for the JONSWAP and Bretschneider spectrum is set to 1.75 m. The point model uses discretised spectra to calculate u_b. For the discretisation 300 frequency bands were used. They were evenly spread between $f = 0.02$ s^{-1} and $f = 0.5$ s^{-1}, the left and right cut-off frequency boundary (f_L and f_R). These values are chosen specifically to minimize the energy loss by the discretisation to less than 1% for every spectrum. Furthermore, for the bulk method not the pre-set value of H_{rms} is used but Equation 2.10 recalculates the H_{rms} value for the bulk method.

symbol	value	meaning	symbol	value	meaning
H_{rms}	1.75 m	root-mean-square wave height	N	300	number of discretisation bands
T_p	8 s	peak period	f_L	0.02 s^{-1}	left cut-off frequency
h	20 m	water depth	f_R	0.5 s^{-1}	right cut-off frequency

Table 3.2: An overview of the default values used in the point model. When other values are applied it is stated specifically in the results.

3.2 Verification with field data

3.2.1 Field data

The spectral method is complementary to the bulk method because the spectral method also considers the shape of the wave spectrum. Consequently, the physical agreement of the calculated u_b by the spectral method should be larger than when the bulk method is used. To determine the size of this improvement both methods are verified using field data.

For the verification a measuring time series of the surface elevation is combined with a velocity measurement at the bottom. The surface elevation measurement will be used to determine u_b by the spectral and bulk method. Their values will be compared with the u_b determined by the velocity measurement which is in this study defined as the correct value. The measurements were taken close to the Sand Motor mega nourishment (see Figure 3.1). The surface elevation was measured by a directional waverider of Rijkswaterstaat positioned at ($52°2'53.16$ N, $4°9'29.76$ E) from 01-02-2013 till 01-04-2013. The waverider is part of Rijkswaterstaat's ongoing measurement program of the Dutch North Sea. The vertical position of the waverider was measured as function of time with a frequency of 1.28 Hz.

As part of the research by *Meirelles et al.* [2015] the near-bed (∼0.5 m from the bed) flow and pressure were measured with a sampling frequency of 8 Hz. To measure the velocity and pressure an ADV (Acoustic Doppler Velocimetry) was attached to a bed-frame, named NEMO Lander, and placed on the bed at a depth of -12 m NAP (Dutch datum at approximately mean sea level). The measurements were taken from 11-02-2013 until 03-03-2013 and were located at ($52°4'12.00$ N, $4°10'37.20$ E). For a more detailed explanation of these measurements one is referred to *Meirelles et al.* [2015].

3.2.2 Data treatment

Before the time signals of the vertical elevation and velocity signal can be used to determine u_b the errors need to be removed and the wave induced spectra need to be extracted. The velocity signal does not contain any measurement at which no value was stored. However, the signal of the

Figure 3.1: Google earth map of the measuring site. The bottom topography is added using OpenEarth-Tools in combination with the vakloding of 2011. The surface elevation measurements were obtained at the dot labelled Wave Buoy and the bottom velocity measurements were obtained at the dot labelled Nemo Lander.

vertical elevation contained 598 moments at which no measurements were taken. A signal with a constant measuring interval is required to be able to determine u_b. The errors are replaced by a value obtained from linear interpolation of the previous and next value which is not an error, to reconstruct the constant measuring interval. The applicability of this method decreases when the number of sequential errors increases. Nevertheless, this method is applied independent of this property because the total number of data points is 2.417.741 and the number of errors grouped in 3 or more subsequent missing values is only 41. Also, 10 measurements were classified as errors and replaced because their value was unrealistic, the smallest of these error measured a vertical displacement of 50 m from mean sea level.

The wave induced spectra need to be extracted from the time signals because other physical processes are also effecting the surface elevation and velocity, for example tides. To determine the wave induced spectra, the time signals are split in segments of 20 minutes. The duration of each segment needs to be long enough to capture the hydrodynamic conditions but not too long because the hydrodynamic conditions need to be stationary. These segments are divided into 9 burst of 4 minutes. As a results, the burst overlap each other for 50 % (see Figure 3.2). In general, 10 burst would be used [*Thomson and Emery*, 2014], but in this particular case is the measuring frequency such that the number of measuring points per burst would change if 10 burst were used instead of 9. The Fourier spectrum of each of these 9 signals was calculated. The 9 filtered spectra were averaged to smoothen the spectra. The wave induced spectrum was defined as the energy density between 0.05 Hz and 0.5 Hz based on the frequency range of wind-generated waves [*Holthuijsen*, 2007]. The rest of the energy in the spectra is removed by applying an ideal non-causal band-pass filter, which is visualized as a block function in the frequency domain [*Baher*, 2001]. For the measured velocity it resulted into a measured velocity density for each frequency in the x and y-direction ($\bar{S}_{uu,i}$, $\bar{S}_{vv,i}$). These energies can be summed linearly to obtain the measured velocity density ($\bar{S}_{uv,i} = \bar{S}_{uu,i} + \bar{S}_{vv,i}$). For the surface elevation the averaged wave energy density is found ($\tilde{E}_i$) (see Figure 3.3). The figure indicates that the boundaries of the wave induced spectrum were

chosen correctly to represent the waves. Due to the averaging procedure an (assumed to be small) error arises because the 9 bursts are not statistically independent.
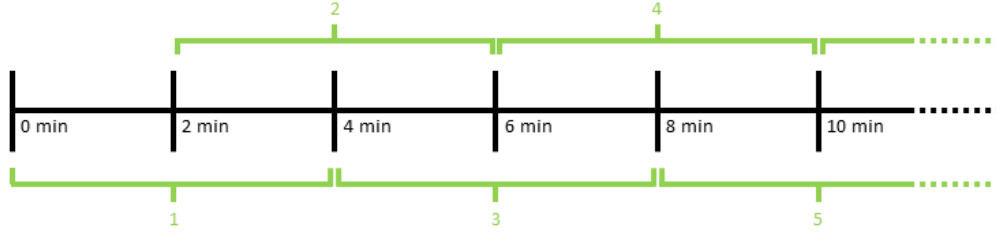

Figure 3.2: A graphical representation of the defined overlap. The first 10 minutes of a 20 minute segment is shown containing 5 bursts. The first and last 2 minutes of each 20 minutes segment is exclusively used by the first and last burst.
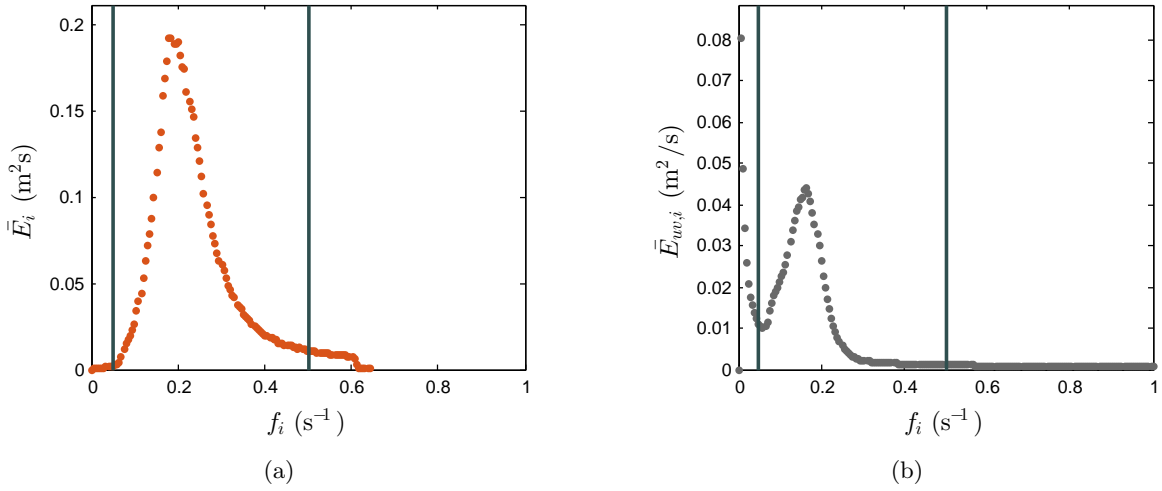

Figure 3.3: Panel (a) shows the discrete energy density ($\tilde{E}_i$) as a function of the discrete frequency (f_i) based on the surface elevation measurement. Panel (b) contains the discrete velocity density ($E_{uv,i}$) as a function of f_i. The time signal contains 1414 segments of 20 minutes and the shown spectra are the averaged spectra over the 1414 segments. The vertical lines in both panels indicate the left (f_L) and right (f_R) cut of boundary of the spectrum. The energy and velocity variance density between these lines are defined as the wave induced part of the spectrum in this research.

3.2.3 Bottom orbital velocity amplitude

The spectra are used to determine 4 values of u_b: (i) based on measured velocity ($u_{b,m}$); (ii) using the spectral method combined with the measured wave spectrum ($u_{b,s}$); (iii) calculated by the spectral method assuming a JONSWAP spectrum ($u_{b,s,J}$) and (iv) determined by the bulk method ($u_{b,b}$). The value of $u_{b,s,J}$ is determined because two differences between $u_{b,s}$ and $u_{b,b}$ can be identified: the consideration of the spectral shape and the dependency of T_p. Consequently, the improvement by the spectral method in physical agreement of u_b is related to both properties. The value of $u_{b,s,J}$ considers a spectral shape but is still dependent on T_p. The smoothing procedure is also applied because of the dependency of T_p. The value of $u_{b,m}$ and $u_{b,s}$ will barely change

because the energy in the spectra is barely influenced by the smoothing procedure. The procedure influences the value of T_p because it reduces the local maxima in each spectrum and amplifies the global maxima. Consequently, the value of $u_{b,b}$ and $u_{b,s,J}$ are effected.

The 4 values of u_b were calculated using different methods. The value of $u_{b,m}$ was calculated by

$$u_{b,m} = \sqrt{2 \sum_i \bar{S}_{uv,i} \Delta f} \tag{3.1}$$

with Δf the size of a frequency band [*Madsen*, 1994]. For the value of $u_{b,s}$ the point model is used, i.e., Equation 2.9. This equation is alos used for $u_{b,s,J}$ but instead of the measured energy distribution it is calculated by Equation 2.6. For $u_{b,b}$ Equation 2.11 is applied. When the depth (h) was required in the calculation the 20 minutes averaged pressure was used to determine h. The entire procedure lead to a value of $u_{b,m}$, $u_{b,b}$, $u_{b,s}$ and $u_{b,s,J}$ for each 20 minutes.

3.2.4 Time series

Based on measurements of the surface elevation, water depth and bottom velocity the values of h, H_{rms}, T_p and $u_{b,m}$ were determined for each time segment of 20 min (see Figure 3.4). Also, the measured wind velocity 10 m above the surface (v_{10}) is shown in this figure. In the time series of h the tidal elevation is clearly visible. It shows a semi-diurnal period with a daily inequality. Between 13-02 and 14-02 a setdown occurred resulting from the wind (see Figure 3.4(b)).

The strong correlation between H_{rms} and v_{10} indicates that the waves are mostly generated by the local wind (see Figure 3.4(b)). At several moments in time, the values of H_{rms} and v_{10} are not correlated, for example at 18-02 and at 02-03. At 18-02 the wind direction, not shown in this report, is offshore directed and because of that the fetch length is limiting rather then the wind velocity. The value of H_{rms} is much higher than expected based on v_{10} at 02-03, most likely because these waves are swell waves.

Surprisingly, H_{rms} and T_p were poorly correlated in the measurements (see Figure 3.4(b) and Figure 3.4(c)). The measured wave spectra still contain several local maxima despite of the smoothing. The energy of theses local maxima is comparable but the difference in frequency is large. Therefore, a small change in a local maxima can result in a different global maxima and a large switch of T_p.

The values of $u_{b,m}$ show no correlation with T_p. The absence of the correlation between T_p and $u_{b,m}$ can again be attributed to the peakiness of the spectrum. The figures shows a correlation between H_{rms} and $u_{b,m}$ which was expected because higher waves (hence a higher H_{rms}) should result in a higher wave induced bottom velocity (hence a higher $u_{b,m}$). The correlation is especially visible around the peaks at 14-02, 24-02 and 01-03. It indicates that the extraction procedure is sufficient to determine $u_{b,m}$.

3.3 Application complex geometry

To investigate the effects of the spectral method on the modelled morphodynamic behaviour of an ebb-tidal delta two schematisations in Delft3D are considered. The first one, discussed in this section, contains a complex geometry but morphological changes are not considered. The second schematisation, explained in the next section, models a more idealised representation of an ebb-tidal delta and it focusses on morphological changes.

The complex geometry of the Vlakte van de Raan, located in the Western Scheld estuary, is modelled using the NeVla model (see Figure 3.5) [*Vroom et al.*, 2015]. The schematised bathymetry
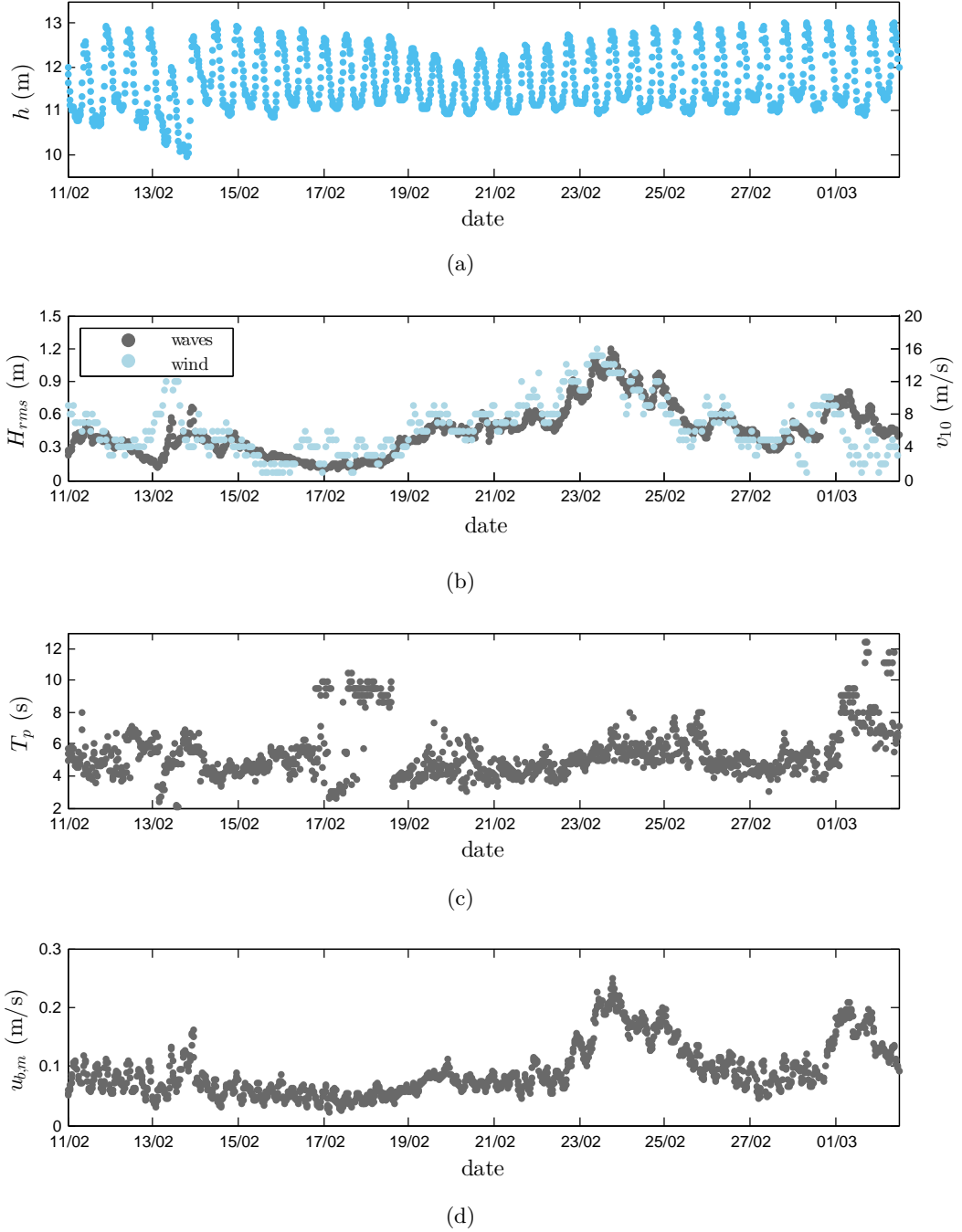
(a)

(b)

(c)

(d)

Figure 3.4: Time signals of several parameters extracted from the measured bottom velocity and measured surface elevation. Panel (a) shows the 20 min averaged water depth (h), panel (b) the root-mean-square wave height (H_{rms}), panel (c) the peak period (T_p) and panel (d) the measured bottom orbital velocity ($u_{b,m}$). The values of T_p, H_{rms} and $u_{b,m}$ are based on the 20 min segments. Panel (b) also contains the hourly averaged wind velocity measured 10 m above the surface (v_{10}).

is based on the measurements of *Hoefsloot and Volleberg* [2014] for the year 2011. The bathymetry used in the flow and wave module are slightly different due to the difference in grid resolution. Furthermore, the numerical grid used for the wave calculation does not cover the entire domain (see Figure 3.6). The upstream part of the river is not considered because the wave height becomes

small enough to neglect waves. The resolution of the numerical grid changes over the domain. In the estuary, the resolution of the grid in the flow module varies between $1/100$ m^{-1} and $1/200$ m^{-1}. The resolution increases further upstream and decreases more offshore. The size of the grid cells used in the wave calculation are a factor two larger than the cells in the flow calculation but the spreading of the cells is identical.
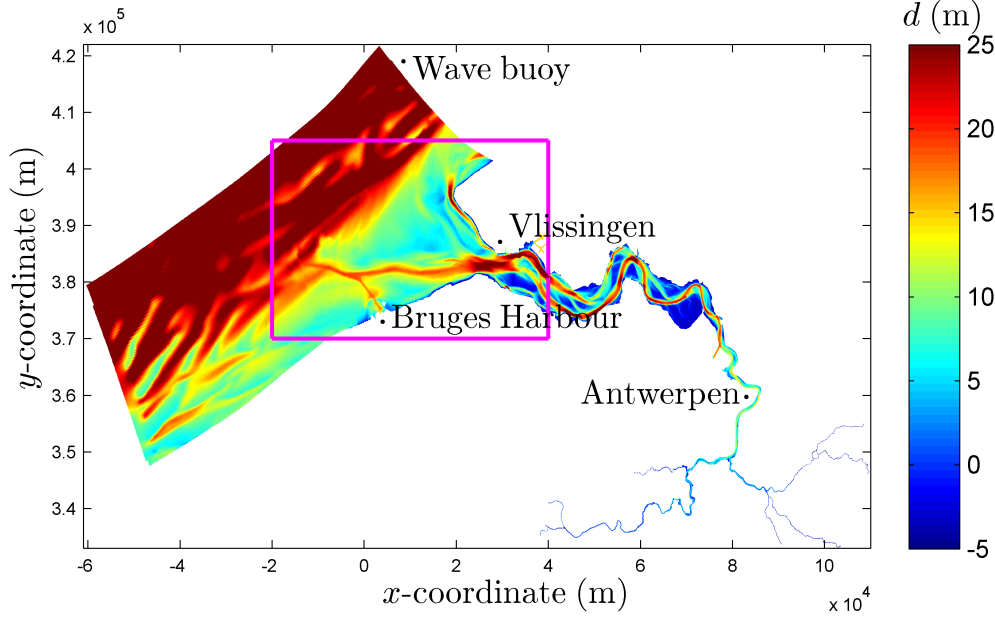
Figure 3.5: The schematised bathymetry used for the complex geometry study. The colours indicate the bottom depth (d). The black dot labelled wave buoy shows the locations of the wave bouy used to determine te boundary conditions. The magenta lines indicate the frame which will be used for the results.
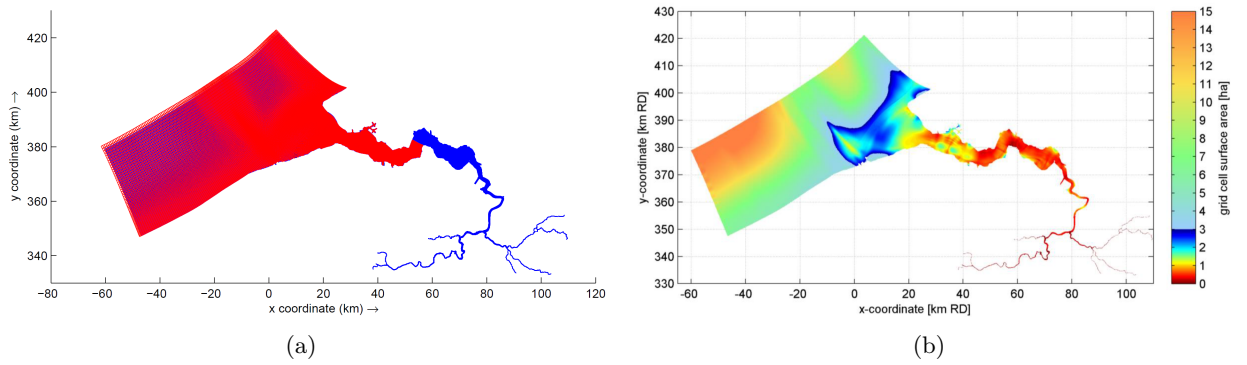
Figure 3.6: In panel (a) the numerical grid for the flow (red) and wave (blue) calculation is presented. Panel (b) illustrates the resolution of the flow grid (reprint from *Vroom et al.* [2015]).

The wave frequency spectrum, wave direction and time are also discretised. The frequency spectrum is discretised into 24 logarithmically distributed bins between 0.05 s^{-1} and 1 s^{-1}. The directional space is discretised by 36 homogeneously distributed directions. In the flow module a time step Δt of 15 s is used. This is combined with an hourly updated steady state wave field from the wave module.

The boundary conditions used in this study are based on measurements and large scale model simulations of the North Sea. The flow boundary conditions located at the seaward side are extracted from the ZUNO model for the year 2006 [*Zijl et al.*, 2013]. The wave boundary conditions are based on the measurements of a wave buoy located at the Schouwenbank (see Figure 3.5). At the three offshore boundaries a JONSWAP spectrum is assumed (see Table 3.1) and in line with this spectrum a T_p and H_{rms} are prescribed. A closed boundary is used for the river side of the wave module. Additionally to these boundary conditions, wind is taken into account. The wind velocity is taken from the KNMI[1] measuring station located in Vlissingen.

Several parametrisations are used to model complex physical processes. The bed shear stress due to waves and current is combined using the formulation of *Soulsby et al.* [1993] using the parameters of *Fredsøe* [1984]. The individual stresses are calculated using a location dependent manning coefficient [*Manning et al.*, 1890] (see Figure 3.7). In the wave module bottom friction, white-capping, wave breaking and non-linear triad wave interaction are taken into account using *Hasselmann et al.* [1973], *Komen et al.* [1984], *Battjes and Janssen* [1978] and *Eldeberky and Battjes* [1996]. Furthermore, the generation of $\tilde{E}$ by wind is taken into account.
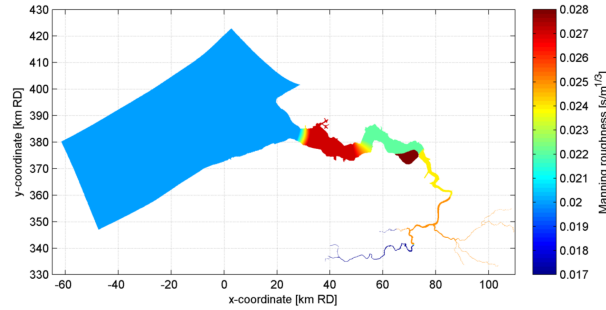
Figure 3.7: The location dependent manning coefficient.

To investigate the effect of the spectral method on a complex geometry 4 simulations are conducted. Simulation 1 and 3 use the bulk method and Simulation 2 and 4 the spectral method. Furthermore, Simulation 1 and 2 represents calm weather conditions and simulation 3 and 4 use parameter values typical for storm conditions (see Table 3.3). The parameters which are changed to model storm or calm weather conditions are the bulk wave parameters and wind velocity (see Table 3.4). The values for the other parameters, which are similar for each simulation are given in Table 3.5.

Method Weather and wave conditions	Bulk	Spectral
Calm weather conditions	Simulation 1	Simulation 2
Storm conditions	Simulation 3	Simulation 4

Table 3.3: An overview of the different simulations with the complex geometry

---

[1]The Royal Netherlands Meteorological Institute (KNMI) is the Dutch national weather service

physical quantity	calm weather conditions	storm conditions	meaning
H_{rms}	0.84 m	1.80 m	root-mean-square wave height
T_p	5.57 s	6.96 s	peak period
θ_p	242.8°	248.9°	dominant wave direction

Table 3.4: The bulk wave parameters for calm weather and storm conditions.

symbol	value	meaning	symbol	value	meaning
f_L	0.05 s^{-1}	left-cut off frequency	ρ	1023 kg m^{-3}	water density
f_R	1 s^{-1}	right-cut off frequency	p	0.4	soil porosity
f	1.16 $\cdot 10^{-4}$ s^{-1}	Coriolis parameter	D_{50}	200 μm	grain diameter
Δt	15 s	time step	ρ_{air}	1.205 kg m^{-3}	air density
M_{fac}	104	morphological factor	ν_e	1 m^{2}s^{-1}	horizontal eddy viscosity
N	24	number of frequency bands	D_H	1 m^{2}s^{-1}	horizontal eddy diffusion coefficient

Table 3.5: An overview of the different parameters and their value used for the simulations of complex geometry study

3.4 Idealised delta formation

To investigate the effects of the spectral method on the morphological changes of an ebb-tidal delta an idealised schematisation is treated. The schematisation of *Ridderinkhof et al.* [2016b] is applied. It consists of a back-barrier basin (size: 9 km by 3.5 km) connected by a tidal inlet (size: 800 m by 1.3 km) to the open sea (size 36 km by 13.5 km) (see Figure 3.8). The flow module and the wave module use a different discretisation. However, both grids become finer closer to the tidal inlet because in this area the hydrodynamic variations and morphological changes are larger. (see Figure 3.9). The finest grid has a resolution of $1/50$ m^{-1} in both modules. Furthermore, the resolution of the coarser grid located seaward is $1/450$ m^{-1}. The grids of the basin have a resolution of $1/150$ m^{-1} and $1/450$ m^{-1} for the flow and wave module. The wave module contains a third grid with a resolution of $1/1350$ m^{-1}. This grid is used to reduce the shadowing effect of the incoming waves.

Boundary conditions for the current, waves and sediment transport need to be defined for the open boundaries. For the current a water level with an amplitude A, a frequency of ω_{M2} and a phase difference $\Delta\phi$ in the x-direction is set on the northern boundary. For the cross-shore boundaries a Neumann boundary is used. In the wave domain only the northern boundary needs to be defined. A JONSWAP wave spectrum is used for this boundary (see Table 3.1), with a dominant direction θ_p. Furthermore, a directional spreading with a cosine power of 4 is used. For the suspended sediment transport a zero-concentration gradient is applied on the open boundaries.

For the idealised schematisation slightly different physical processes are considered then for the complex geometry. Instead of a manning coefficient the friction coefficient is determine by *van Rijn* [2007a] combined with *Colebrook and White* [1937] to determine the drag coefficient by the current. In the wave calculation the same sources and sinks are considered as for the complex geometry except wind and non-linear triad wave interaction.

To investigate the effects of the spectral method two Delft3D simulation are defined. The simulations use similar settings (see Table 3.6) but differ in the calculation of u_b. Run 1 and Run 2
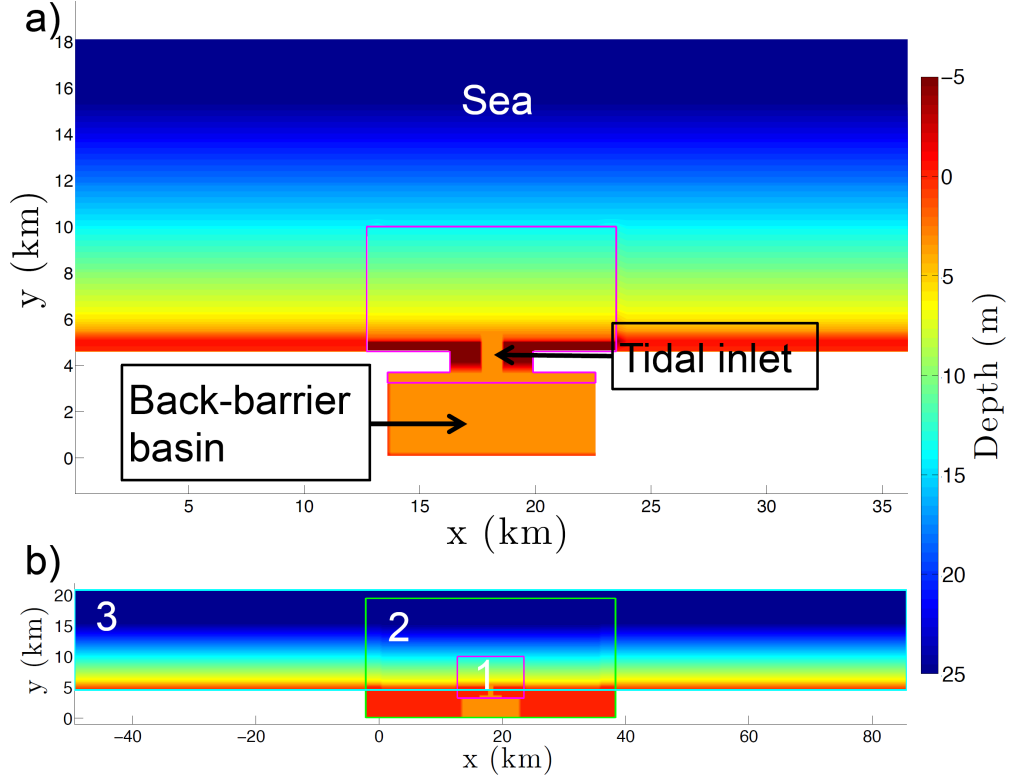
Figure 3.8: Panel (a) shows the initial morphological domain of the flow calculation used for the idealised delta formation with the colours indicating bottom depth (d). The magenta lines indicates a change in grid resolution of the flow module. Panel (b) visualises the initial morphological domain of the wave module. It consists of three nested grids indicated by the green and the magenta lines. *Reprint from Ridderinkhof et al. [2016b])*

.

both use the bathymetry given in Figure 3.8. However, Run 1 uses the bulk method to calculated u_b and Run 2 the spectral method.

symbol	value	meaning	symbol	value	meaning
H_{rms}	0.85 m	root-mean-square wave height	N	24	number of frequency bands
T_p	5.75 s	peak period	A	1 m	tidal amplitude
θ_p	335°	dominant wave direction	D_H	1 m^{2}s^{-1}	horizontal eddy diffusion coefficient
$\Delta\phi$	21°	tidal phase difference	ν_e	10 m^{2}s^{-1}	horizontal eddy viscosity
ω_{M2}	1.45 $\cdot 10^{-4}$ s^{-1}	tidal period	D_{50}	250 μm	grain size
f_L	0.05 s^{-1}	left cut-off boundary	p	0.4	soil porosity
f_R	1 s^{-1}	right cut-off boundary	Δt	15 s	time step
f	1.12 $\cdot 10^{-4}$ s^{-1}	Coriolis parameter	M_{fac}	20	morphological factor
ρ	1000 kg m^{-3}	water density			

Table 3.6: An overview of the different parameters and their value used for the ideal delta formation.

Summary: The three different spectral shapes for the point model were introduced. Further-

(a)

(b)
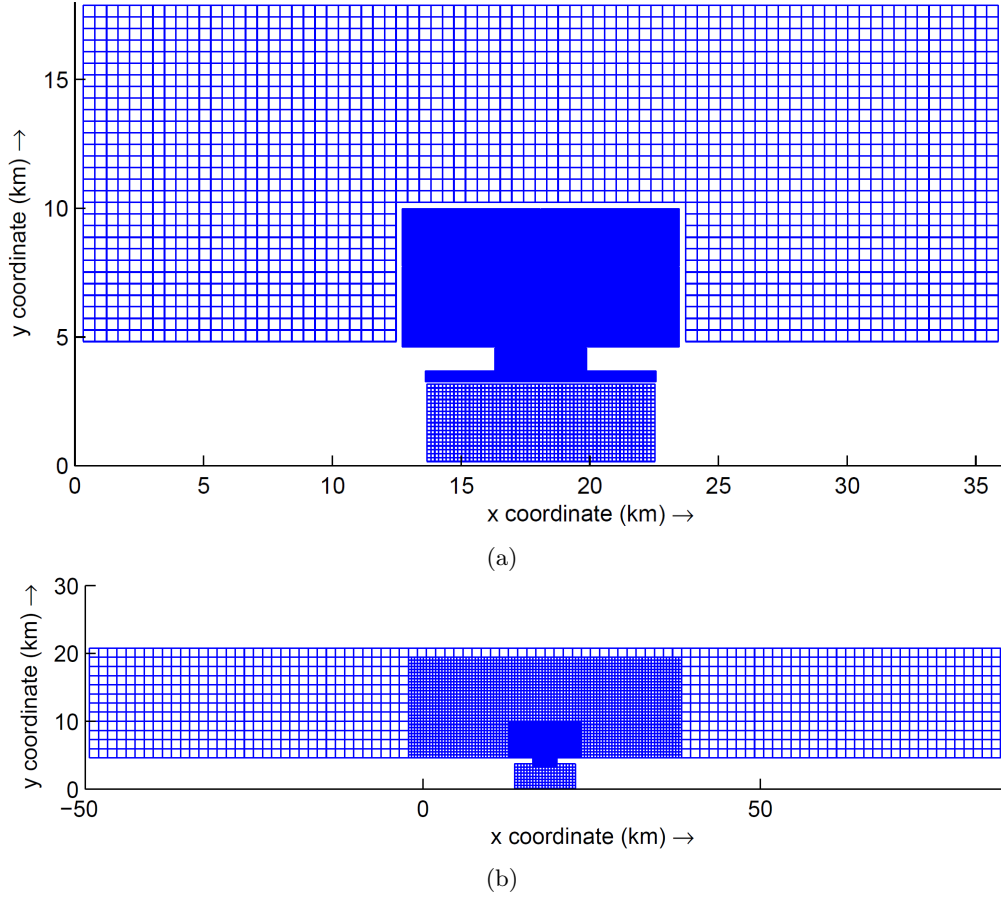
Figure 3.9: In panel (a) the numerical grid for the flow calculation and in panel (b) for the wave calculation.

more, the observation used to quantify the physical improvement by the spectral method, filtering procedure and the measured time series were given. Finally, the two complex schematisations of the ebb-tidal deltas were explained. The next chapter will show and explain the results.

Chapter 4

Results

The results of the models and the measurements are shown and analysed in this chapter. First, the results of the spectral point model, described in Section 2.3 and 3.1, are given in Section 4.1. They are used to investigate the effect of water depth (h), peak period (T_p), root-mean-square wave height H_{rms} and spectral shape (γ) on the bottom orbital velocity (u_b) calculated by the bulk method ($u_{b,b}$) and the spectral method ($u_{b,s}$). The first research question (how do the water depth, root-mean-square wave height, peak period and spectral shape influence the difference between a bottom orbital velocity amplitude calculated using the bulk method and the spectral method?) will be addressed in this section. Section 4.2 evaluates the bulk and spectral method using field data, explained in Section 3.2. The values of $u_{b,s}$ and $u_{b,b}$ are compared with a measured bottom orbital velocities ($u_{b,m}$) to answer the second research question (is the calculated bottom orbital velocity amplitude significantly improved when a spectral method is used instead of a bulk method?). Section 4.3 focusses on the complex geometry, and Idealised delta formation is analysed in Section 4.4. Both Delft3D schematisations were defined in Chapter 3. The modelled results are investigated to answer the third research question (how does the spectral method used to compute the bottom orbital velocity amplitude and subsequent sediment transport influence the modelled morphodynamic behaviour of complex systems compared to the situation when the bulk method applied?) The morphological changes are investigated using the idealised delta study.

4.1 Point model

The point model uses the values for T_p, H_{rms} and γ to construct a theoretical discrete energy density spectrum. The discrete energy density ($\tilde{E}_i$) is converted into a discrete bottom orbital velocity variance density ($\tilde{u}_{b,i}^2$). The results for three spectral shapes is presented in Figure 4.1. The values of $\tilde{E}_i$ and $\tilde{u}_{b,i}^2$ can be interpreted as the contribution in wave energy and local kinetic energy of a particular wave with frequency f_i to the total wave and total kinetic energy. The total wave energy and local kinetic energy determine the values of H_{rms} and $u_{b,s}$. The figure shows that the relative contribution of waves with $f_i > 0.15$ Hz to H_{rms} is smaller than the relative contribution of these wave to $u_{b,s}$. It means that waves with a higher frequency ($> \sim 0.15$ Hz) more strongly influence H_{rms} than u_b. Every spectrum in Figure 4.1 shows this behaviour. Physically, it means that u_b due to a sinusoidal wave with a higher frequency is smaller than due a sinusoidal wave with a lower frequency when the amplitude and water depth are identical in both calculations. Another interpretation is that the reduction of the wave orbital velocity due to the water depth is larger for waves with a higher frequency than for waves with a smaller frequency.

The reduction of the orbital velocity also explains the change in the peak frequency (f_p) between the wave energy density spectrum and the bottom orbital velocity variance spectrum for $\gamma = 1$ (the Pierson-Moskowitz and Bretschneider spectrum). The reduction is frequency dependent and not every frequency contains the same amount of energy. As a result, a change in f_p arises if the difference in reduction between the difference frequencies is large enough to compensate for the absolute difference in $\tilde{E}_i$ between the different frequencies. No f_p shift occurs in the JONSWAP spectrum because it is narrower. Therefore, the difference in reduction is not large enough to compensate for the difference of $\tilde{E}_i$ around f_p.

For other depths, the point model reveals that the value of $u_{b,s}$, found by a discrete integral

(a)

(b)
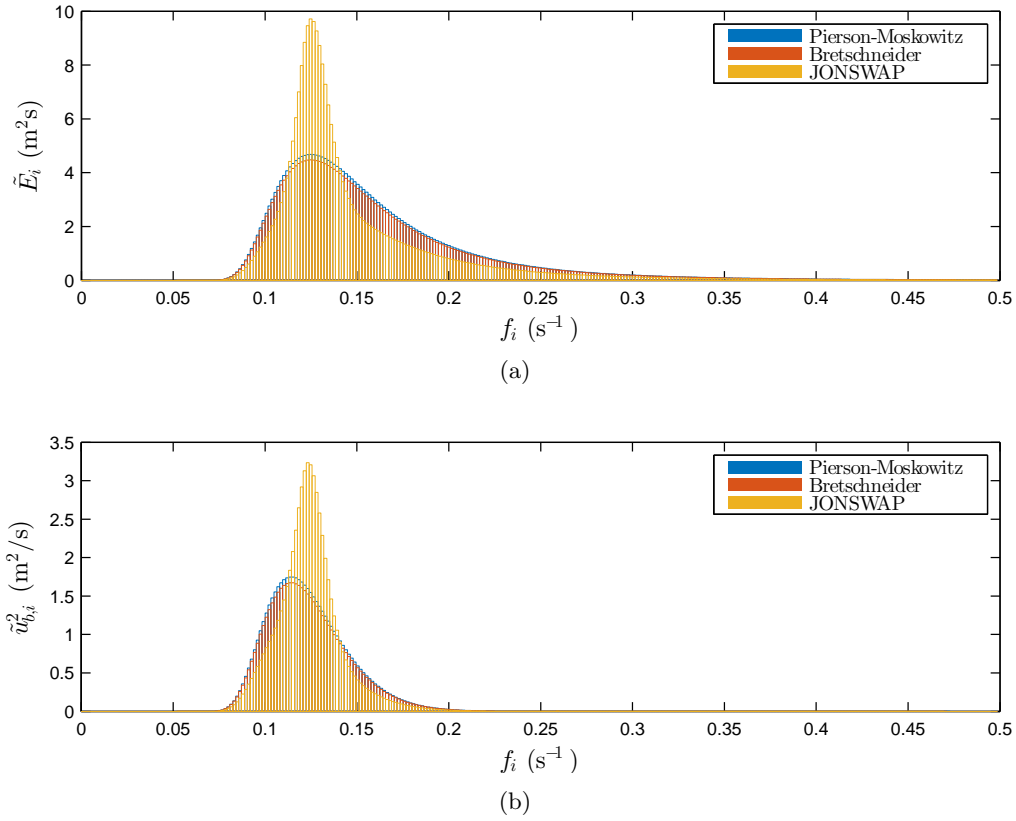
Figure 4.1: (a) The discrete energy density spectrum ($\tilde{E}_i$) and (b) the discrete bottom orbital velocity variance density spectrum ($\tilde{u}_{b,i}^2$) as a function of the discrete frequency (f_i) for three different spectrums: Pierson-Moskowitz, Bretschneider and JONSWAP (see Table 3.1). A depth of 20 m is used (see Table 3.2).

over the velocity variance spectrum, is smaller than the value of $u_{b,b}$ for $T_p = 8$ s (see Figure 4.2(a)). As was explained in the previous paragraph, the reduction of the wave orbital velocity by the water depth is frequency dependent. The orbital velocities by the high frequency waves are reduced more than for waves with a lower frequency. The spectral method considers a collection of waves opposed to the bulk method which uses a single wave with a period T_p. Consequently, the wave orbital velocity by waves with a longer period ($> T_p$) is reduced less by the water depth compared to the reduction when the bulk method is used. On the other hand, for waves with a shorter period ($< T_p$) the reduction is larger. For $T_p = 8$ s the total reduction is larger if the entire wave spectrum is included than when only the peak period is considered. In other words, the decrease in the reduction of the bottom orbital velocity by the water depth for waves with a larger period can not compensate for the increase in the reduction of the orbital velocity of the waves with a shorter period. As a result, the value of $u_{b,s}$ is smaller than $u_{b,b}$.

The effect of the depth is similar for the three spectra for $T_p = 8$ s, but small differences occur. The difference between $u_{b,s}$ and $u_{b,b}$ is smaller for the JONSWAP spectrum than for the Pierson-Moskowitz and the Bretschneider spectrum. This is because the JONSWAP spectrum has a narrower shape. The values of $u_{b,s}$ and $u_{b,b}$ are slightly larger for the Pierson-Moskowitz spectrum than for the other two spectra. This arises from the empirical relation ($H_{rms} = 0.0282T_p^2$) used in the Pierson-Moskowitz spectrum (see Section 3.1). The Pierson-Moskowitz spectrum is not dependent on the value of H_{rms} due to this relation. On the other hand, one could also reason that the value of H_{rms} is adjusted automatically to the value of T_p. The automatical adjustment

(a)

(b)
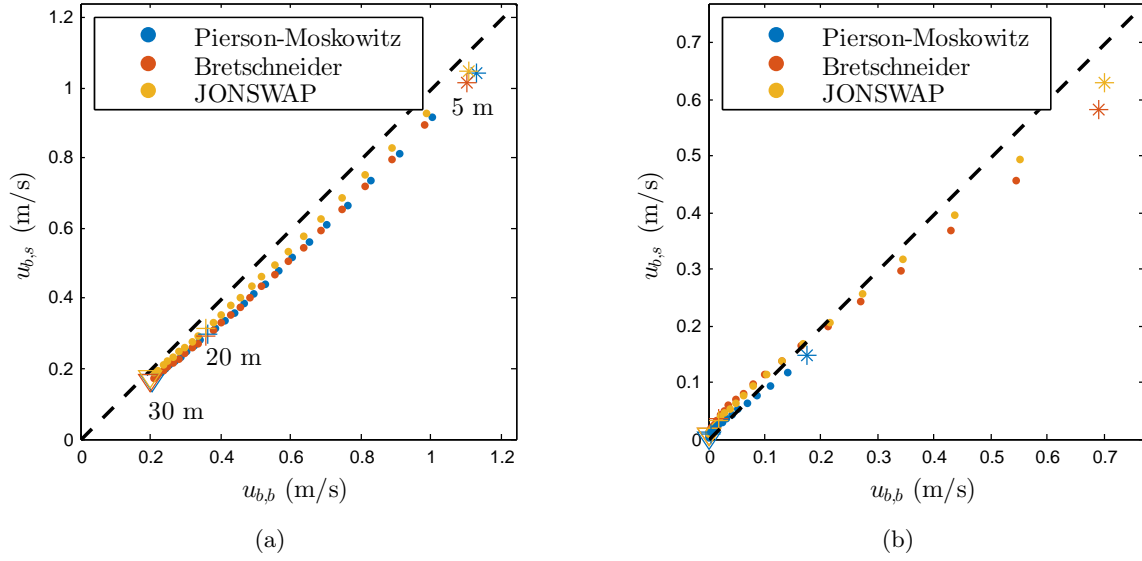
Figure 4.2: Plots showing the bottom orbital velocity calculated by the spectral method ($u_{b,s}$) versus the bottom orbital velocity calculated by the bulk method ($u_{b,b}$). In each panel the depth (h) decreases from left to right from $h = 30$ m till $h = 5$ m in steps of 1 m. The values of u_b at a depth of 5 m, 20 m and 30 m are indicated with "$*$", "$+$" and "$\bigtriangledown$", respectively. The numbers in panel (a) indicate this depth. The dashed line is the line of perfect agreement ($u_{b,s} = u_{b,b}$). The Bretschneider and the JONSWAP spectrum use a root-mean-square wave height (H_{rms}) of 1.77 m (see Table 3.2). Panel (a) uses a peak period (T_p) of 8 s and panel (b) of 4 s.

results in a higher value of H_{rms} (1.80 m) than used for the other spectra ($H_{rms} = 1.77$ m). The value of u_b is linearly dependent on H_{rms} and because of that the value of $u_{b,s}$ and $u_{b,b}$ are slightly larger for the Pierson-Moskowitz spectrum.

A change in T_p from 8 to 4 seconds strongly influence the behaviour of u_b (see Figure 4.2). The frequency-dependent reduction results in larger or smaller values of $u_{b,s}$ than $u_{b,b}$ for $T_p = 4$ s, depending on the value of h. As was explained in previous paragraph, when the decrease in reduction of waves with a larger period is smaller than the increase in reduction of the short period waves then $u_{b,s} < u_{b,b}$. Whereas, $u_{b,s} > u_{b,b}$ indicates that the decrease in reduction of the waves with a larger period compensates the increase in reduction of the waves with a shorter period.

When the value of T_p is changed, the value of $u_{b,s}$ for the spectra is strongly influenced. The values of u_b based on the Pierson-Moskowitz spectrum are much smaller for $T_p = 4$ s compared to the other spectra with the same value of T_p. As was explained in the previous paragraph, the Pierson-Moskowitz spectrum contains an empirical relation which implies an automatic adjustment of H_{rms} to the value of T_p. Due to this property, the H_{rms}, supposedly used for the Pierson-Moskowitz spectrum is 0.45 m for $T_p = 4s$ and much smaller than the 1.77 m used of the Bretschneider and JONSWAP spectrum. The effect of T_p and h on the ratio $u_{b,s}$ to $u_{b,b}$ is difficult to analyse due to the non-linear influence on u_b.

Figure 4.3 visualises the dependency of T_p and h on u_b. The figure shows that for every value of T_p the ratio $u_{b,s}$ to $u_{b,b}$ can be larger as well as smaller than 1, depending on h. The value of h that results in a ratio larger than 1 increases for increasing T_p. For every value of T_p a minimum in the ratio can be observed, for example at $h = 17$ m for $T_p = 7$ s. Furthermore, for every T_p a steep increase of the ratio occurs for increasing h. The steep increase in the ratio results from the steep decrease in the value of $u_{b,b}$ which is due to the steep increase of $\sinh(k_p h)$

(a)

(b)
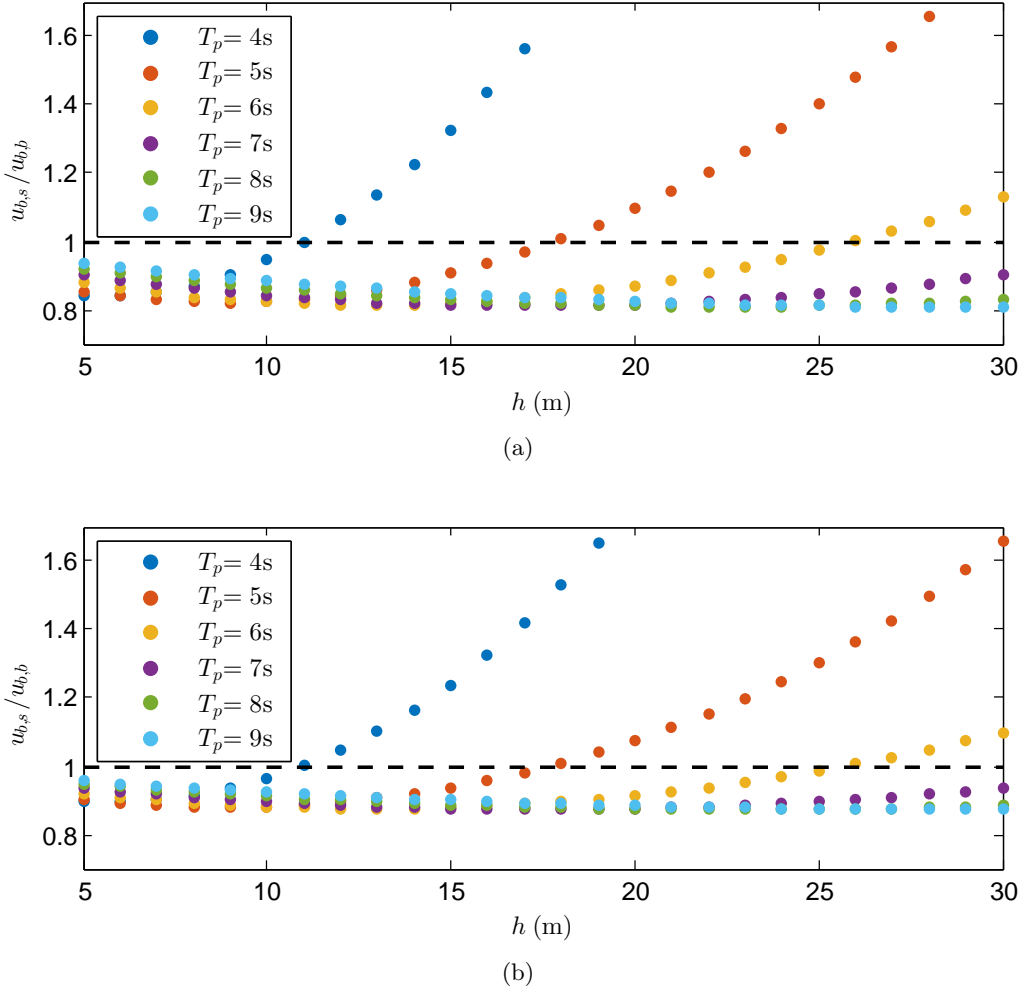
Figure 4.3: Plots of the ratio $u_{b,s}/u_{b,b}$ as a function of depth (h) for different peak periods (T_p). Here $u_{b,s}$ and $u_{b,b}$ between the bottom orbital velocity calculated using the spectral method and the bulk method. The dashed line indicates the line of perfect agreement ($u_{b,s} = u_{b,b}$). For panel (a) the Bretschneider spectrum and for panel (b) the JONSWAP is used to calculate $u_{b,s}$.

The ratio $u_{b,s}/u_{b,b}$ is weakly dependent on the spectral shape. The results for the Pierson-Moskowitz spectrum are identical to the outcome when the Bretschneider spectrum was and for that reason not shown in this report. Their results are identical because the difference between these two shapes is their dependency on $H_r ms$ and the ratio $u_{b,s}$ to $u_{b,b}$ is independent of H_{rms}. The ratios for the JONSWAP spectrum are closer to 1 compared to the ratios using the Bretschneider spectrum. The JONSWAP spectrum is a narrower spectrum than the Bretschneider spectrum (see Figure 4.1(a)). As a result, the difference between a JONSWAP spectrum and a single frequency spectrum is smaller than between a Bretschneider spectrum and a single frequency spectrum. As a rule of thumb it can be stated that the ratio increases for increasing h and decreases for increasing T_p but this rule of thumb does not consider the minimum value of $u_{b,s}/ub, b$. It should be taken into consideration that, although the ratio increases, the absolute difference can become smaller when h increases (see Figure 4.2).

Summary: First of all, the point model constructs a theoretical $\tilde{E}_i$ spectrum based on H_{rms}, T_p and γ and converts it into a $\tilde{u}_{b,i}^2$ spectrum. Secondly, the value of u_b decreases for increasing

depth but increases for larger T_p. Furthermore, the ratio $u_{b,s}$ to $u_{b,b}$ can be smaller or larger than 1 depending on the value of T_p and h, but as a rule of thumb, the ratio increases for larger h and smaller T_p. Finally, the effects of γ were limited when the changes in H_{rms} were taken into account.

4.2 Verification with field data

The measured values of h, H_{rms}, T_p are used to determine $u_{b,b}$ and $u_{b,s}$ and to compare them with $u_{b,m}$. The different values of u_b show that using the spectral method give values of u_b wich are in better agreement with u_{b_m} than when the bulk method is used (see Figure 4.4). The better agreement by the spectral method can be assigned to three differences between the spectral method and the bulk method. First of all, the spectral method takes the frequency-dependent reduction
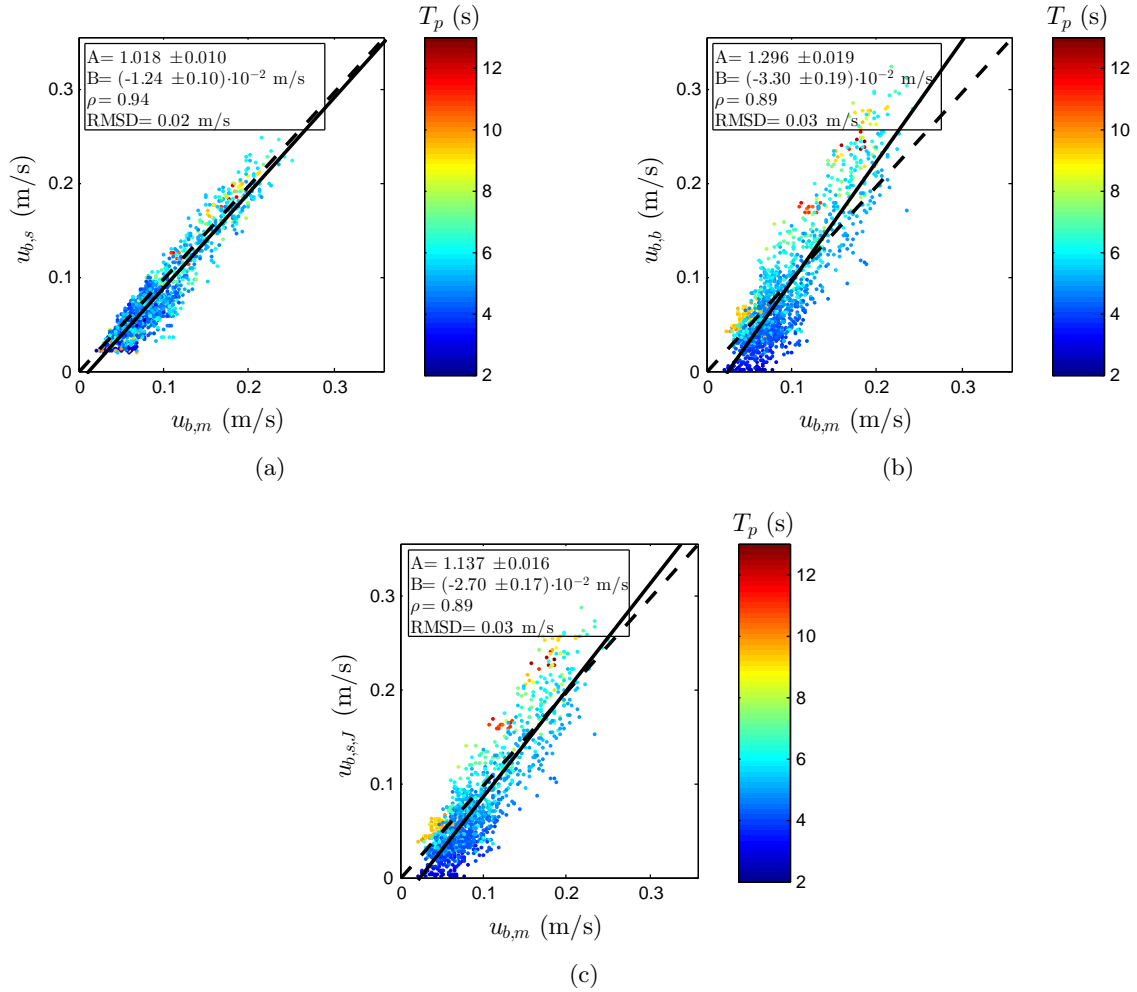
Figure 4.4: Panel (a) shows a scatter plot of the bottom orbital velocity calculated using the spectral method ($u_{b,s}$) versus the measured bottom orbital velocity ($u_{b,m}$). The colour represents the value of the peak frequency T_p. The solid black line indicates the best fit to the line $y = Ax + B$ determined by a least square method. The dashed line indicates the 1:1 line. The boxes shown in the top left corner of each panel show the value of the fit parameters A and B. These boxes also contain the correlation coefficient (ρ) and the root-mean-square difference indicated by RMSD. Panel (b): as in panel (a) but the bottom orbital velocity is determined by the bulk method ($u_{b,b}$). Panel (c): as in panel (a) but the spectral shape is assumed to be a JONSWAP spectrum ($u_{b,s,J}$).

into account. Furthermore, the spectral method considers more measured properties, namely, the measured shape of the wave spectrum. Finally, the spectral method is not dependent on T_p. The value of T_p is poorly correlated with the values $u_{b,b}$ but should be positively correlated with it (see Equation 2.11). To identify the contribution of these differences between the spectral and bulk method the value of u_b is calculated using the spectral method and assuming a JONSWAP wave spectrum ($u_{b,s,J}$). The value of $u_{b,s,J}$ considers the frequency-dependent reduction but does not take into account the measured shape. In addition, it is dependent on the value of T_p.

The agreement between $u_{b,s,J}$ and $u_{b,m}$ is larger than between $u_{b,b}$ and $u_{b,m}$ but smaller than between $u_{b,s}$ and $u_{b,m}$. The errors by $u_{b,s}$, $u_{b,b}$ and $u_{b,m}$ demonstrate that all the three differences are of similar importance but the dependency of T_p can by identified as the major shortcoming of $u_{b,s,J}$. This shortcoming also applies to the bulk method.

The fit parameters A and B, the correlation coefficient (ρ) and the root-mean-square difference (RMSD) support that the spectral method provides more accurate values of u_b than the bulk method. The value of A for $u_{b,s}$ is 1.018 ± 0.010 which makes it not significantly different from 1 assuming an exceedance probability of 5% and assuming that the values of A are normally distributed. The values of A for $u_{b,b}$ and $u_{b,s,J}$ are both significantly different from 1 but the exceedance probability for $u_{b,b}$ is smaller than for $u_{b,s,J}$. The offset indicated by B is significantly different from 0 for every method. It is hypothesised that this is the result of the turbulent kinetic energy (TKE) induced by the background current. The large scale currents are separated from the time signal by the filter procedure. The large scale current generates turbulent kinetic energy at the scales of the wave induced velocity by the turbulent energy cascade [*Pope*, 2001]. This TKE is not filtered out because it has the same frequency range as the wave induced velocity. The effects of the TKE result in a higher value of $u_{b,m}$ because the value of $u_{b,m}$ is determined by the energy in the measured velocity spectrum. The values of ρ and RMSD are as expected based on the values of A. For ρ the closest value to 1 is found for $u_{b,s}$. Additional, the smallest value for RMSD is found for $u_{b,s}$. As a result, the value of $u_{b,s}$ best represents the values of $u_{b,m}$.

Summary: The values of $u_{b,m}$, $u_{b,s}$ and $u_{b,b}$ indicated that the spectral method provided a better agreement with a measured u_b than the bulk method. The values of $u_{b,s,J}$ showed that the dependency of T_p is a major drawback of the bulk method but the errors by neglecting frequency-dependent reduction and the spectral are also significant. The values of A, B, ρ and RMSD support these conclusions.

4.3 Application complex geometry

The Delft3D NeVla model values for h, T_p and H_{rms} typical for the Dutch coast (see Figure 4.5). The results of the complex geometry schematisation produce oscillations due to spin-up but also due to the tides. At $t = 0hrs$, with t the time index after spin-up time, the oscillations due to the spin-up effect are damped out but the variations due to the tides still appear. The results are shown for $t = 20hrs$ because at this moment the current at the Vlakte van de Raan has reached its maximum value in 24 hours. The velocities are higher in the deeper parts of the systems for example in the channels, especially in the narrow estuary mouth (landward of the Vlakte van de Raan).

The patterns of T_p and H_{rms} strongly differ from the shapes shown by h and $|\vec{u}|$ but similarities can be seen. The pattern of H_{rms} is relative smooth. This is due to wave refraction. The values of T_p are related to physical processes which change the shape of the wave spectrum. As a result, the value of T_p changes.

The ratio $u_{b,s}/u_{b,b}$ shows a strong dependency on h, but it is limited influenced by the variations
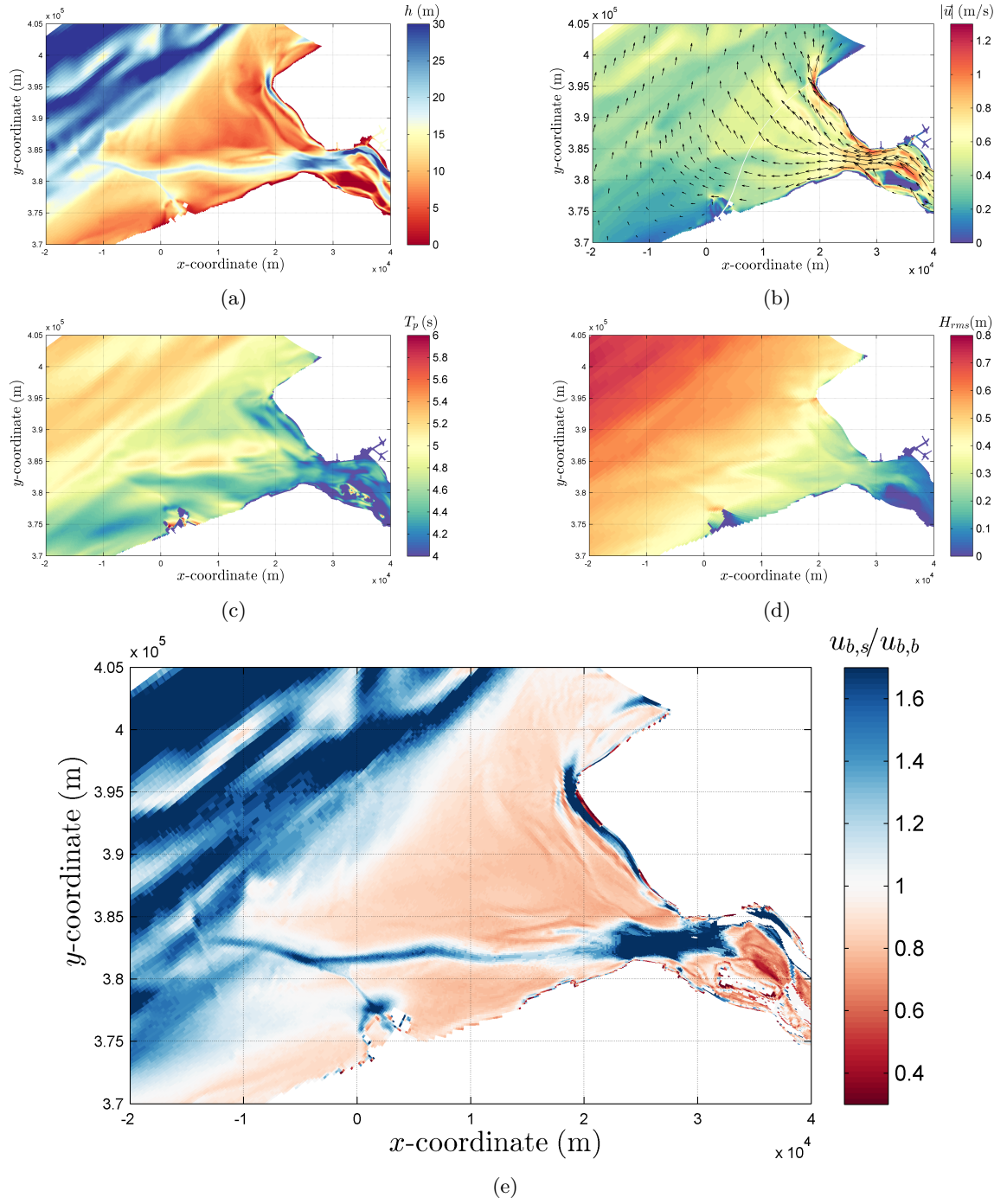
Figure 4.5: Results of the complex geometry 20 hours after spin-up ($t = 20$ hrs) for the calm weather conditions (see Table 3.3). Panel (a) shows the water depth (h). In panel (b) the colour indicates the magnitude of the velocity ($|\vec{u}|$), the arrows are aligned with the local velocity direction and scale with the magnitude of the velocity. The white line crossing the domain indicates the boundary between two grids. The peak period (T_p) is shown in panel (c) and panel (d) displays the root-mean-square wave height (H_{rms}). Panel (e) presents the ratio $u_{b,s}/u_{b,b}$, where $u_{b,s}$ is the bottom orbital velocity calculated by the spectral method and $u_{b,b}$ the bottom orbital velocity determined the bulk method.

in T_p (see Figure 4.5(e)). In the channels of the ebb-tidal delta the value of $u_{b,s}$ is up to a factor 1.6 higher than $u_{b,b}$, similar to the ratios in the offshore areas. On the other hand, on the shoal the bulk method yields a higher value of u_b than the spectral method. These results are in good agreement with the depth dependency of the ratio $u_{b,s}/u_{b,b}$ (see Figure 4.3(b) and Figure 4.5(a)). Due to this agreement an identical explanation can be given to understand the results of the complex geometry as for the results of the point model. The variations in T_p over the domain are poorly shown in the u_b ratio because the relative variation in T_p are smaller than those in h. Namely, T_p changes from $\sim$4 s till $\sim$5.5 s which is a factor 1.375. The depth changes a factor 5, from $\sim$5 m till $\sim$25 m. The individual wave spectra are not shown because the point model indicated that the exact shape of the spectra were of limited importance. The changes in $u_{b,s}$ will effect the shear stresses by waves on the bottom and as a result the sediment transport. This can lead to a morphological change if a gradient in sediment transport arises due the change in stresses.

For the storm conditions (see Table 3.3) similar hydrological patterns were modelled as for the calm weather conditions and an equivalent qualitative good agreement with the point model was observed. The hydrodynamic conditions are shown in Apppendix A because the difference with Figure 4.5(a), 4.5(b), 4.5(c) and 4.5(d) were minimal. The magnitude of T_p and H_{rms} over the domain changed in line with the other boundary values for H_{rms} and T_p for the storm conditions. The pattern of T_p and H_{rms} stayed similar to the calm weather conditions. Furthermore, the pattern of the ratio $u_{b,s}/u_{b,b}$ showed a strong depth dependency.

For the storm conditions, the ratio $u_{b,s}/u_{b,b}$ is closer to 1, i.e. the differences between the bulk method and the spectral method become smaller (see Figure 4.6). For a depth lower than $\sim$8 m, Figure 4.3(b) indicates that an increase in T_p from $\sim$4.7 s to $\sim$6 s (typical T_p over the shoal for the calm weather and storm conditions) would reduce the ratio. This explains why the ratio $u_{b,s}/u_{b,b}$ over the shoal is closer to 1 for the storm condition than for the calm weather conditions. In the channel T_p changes from $\sim$4.4 s for calm weather conditions to $\sim$5 s for the storm conditions. Figure 4.3(b) shows that for depths larger than $\sim$14 m and for these values of T_p the ratio will become closer to 1. The large and distinct difference in depth between the shoal and channel is a decisive property of the system why the ratio of u_b becomes closer to 1 for storm conditions over the entire area.

The agreement between the NeVla model and the point model changed during the tidal cycle. On the other hand, a higher ratio in the deeper parts than in the shallow areas, was conserved. The ratio changed from larger than 1 to smaller than 1 over almost the entire area (see Figure 4.7 and Figure 4.8). These changes show a periodicity close to 12 hours and because of that it is suggested they are related to the tidal current. This hypothesis is further supported by prevalence of these changes in the offshore areas. In these areas, the fluctuations of h due to the tides is small compared with d. This effect is further discussed in Section 5.3.

Summary: The modelled ratio $u_{b,s}/u_{b,b}$ of the NeVla model was in good agreement with the point model. As a result, an identical reasoning as for the point model could be given to explain the results of the NeVla model. Furthermore, for storm conditions the u_b ratio became closer to 1 because of the distinct difference in bottom depth between the shoals and the tidal channels. Finally, difference arose between Delft3D and the point model when other moments during a tidal cycle were investigated.

(a)
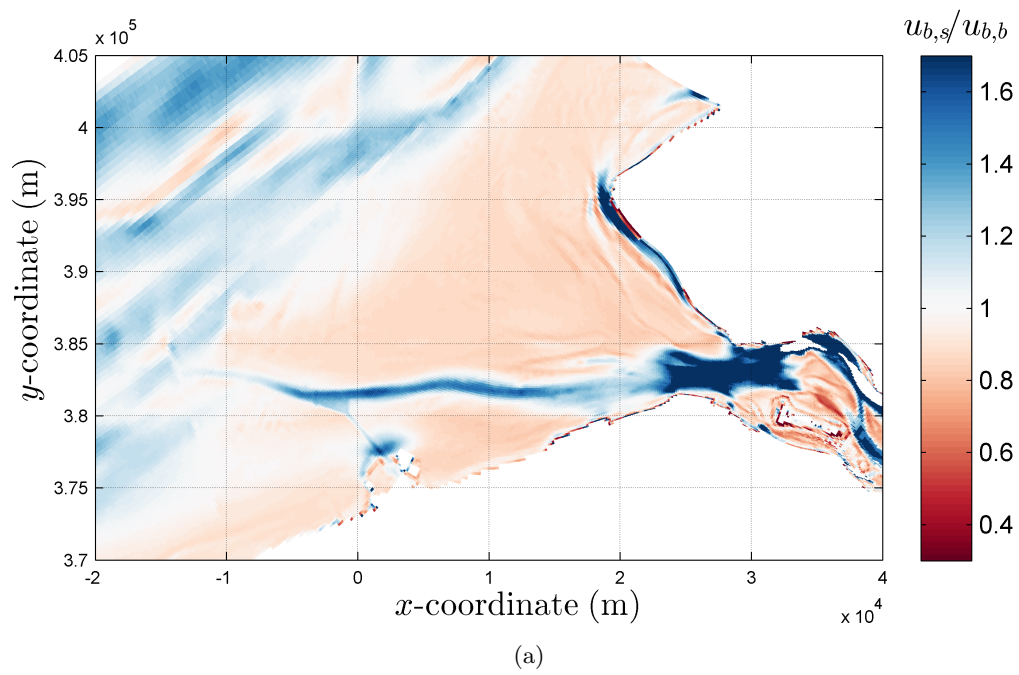
Figure 4.6: As in Figure 4.5(e), but for storm conditions (see Table 3.4).

(a)

(b)
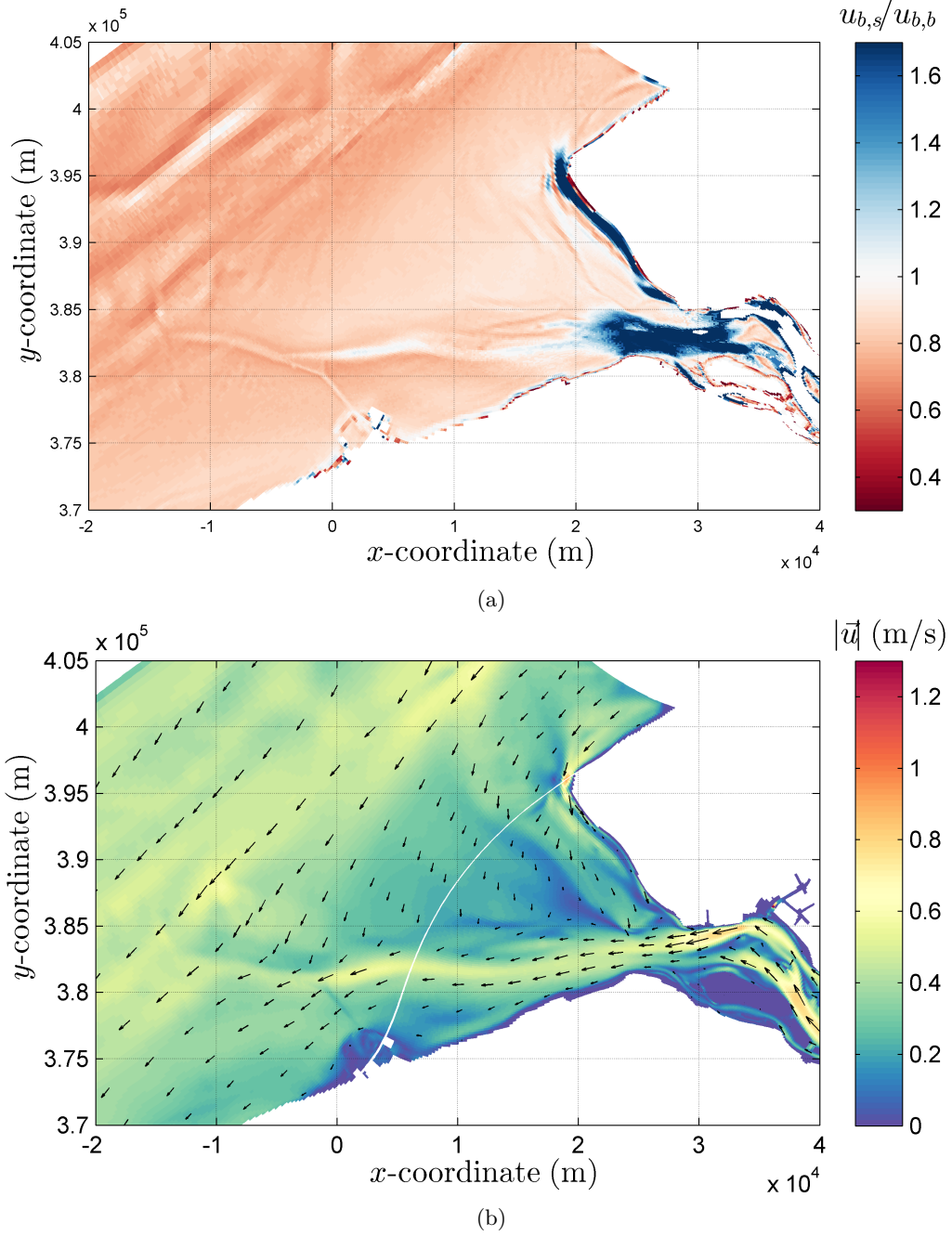
Figure 4.7: Panel (a) as Figure 4.5(e), but for $t = 24$ hrs. Panel (b) as Figure 4.5(b) but for $t = 24$ hrs.

(a)

(b)
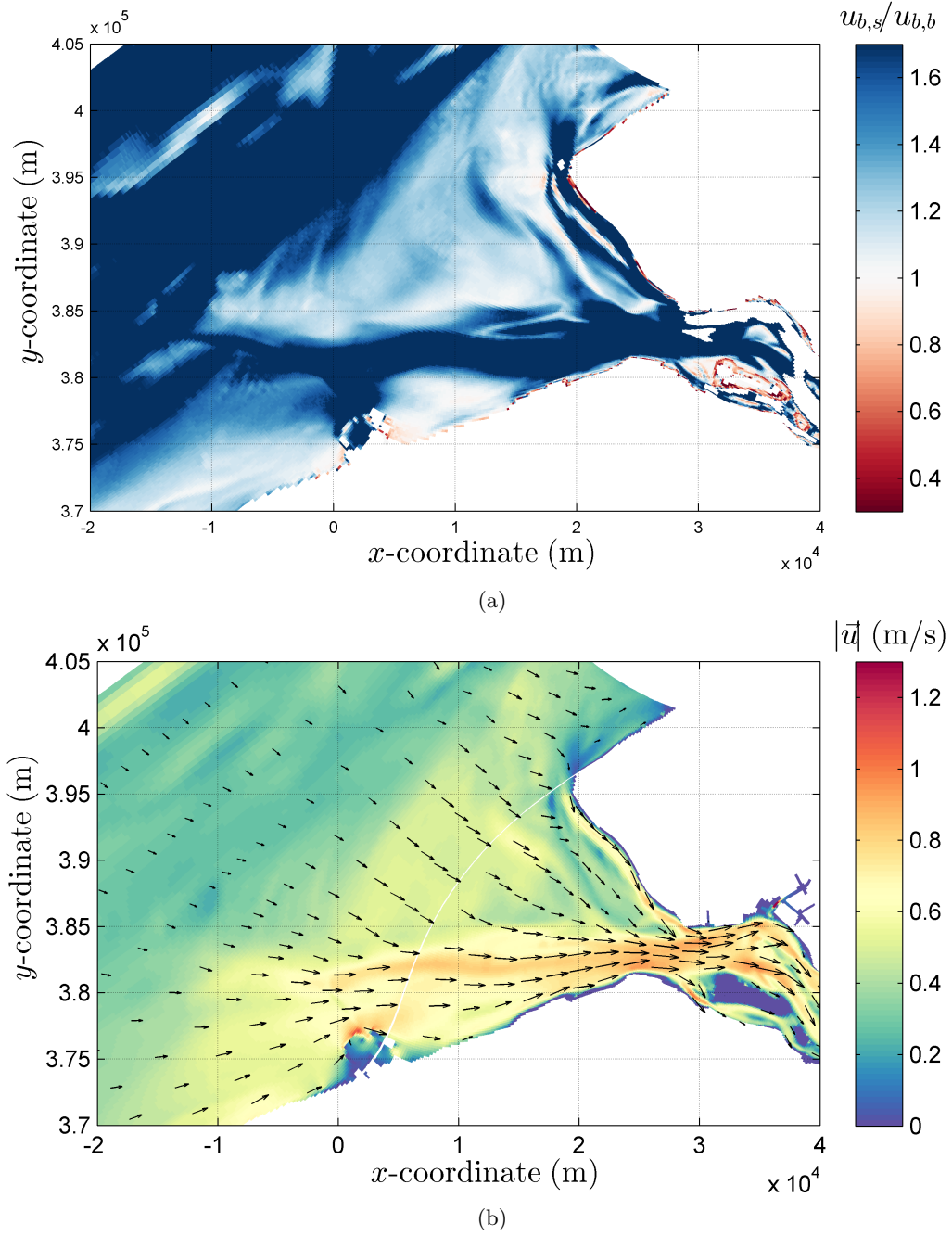
Figure 4.8: Panel (a) as Figure 4.5(e) and panel (b) as Figure 4.5(b) but for $t = 28$ hrs.

4.4 Idealised delta formation

The Delft3D schematisation used to investigate the morphological effects of the spectral method resolves in a dynamically stable ebb-tidal delta (see Figure 4.9). Small variations in the morphology are observed during a tidal cycle but the net effect is negligible when averaged over this cycle. The ebb-tidal delta is orientated into the negative x-direction. This orientation is the result of the phase difference between the cross-shore and alongshore tidal current [*Sha and Van den Berg*, 1993].

(a)

(b)

(c)
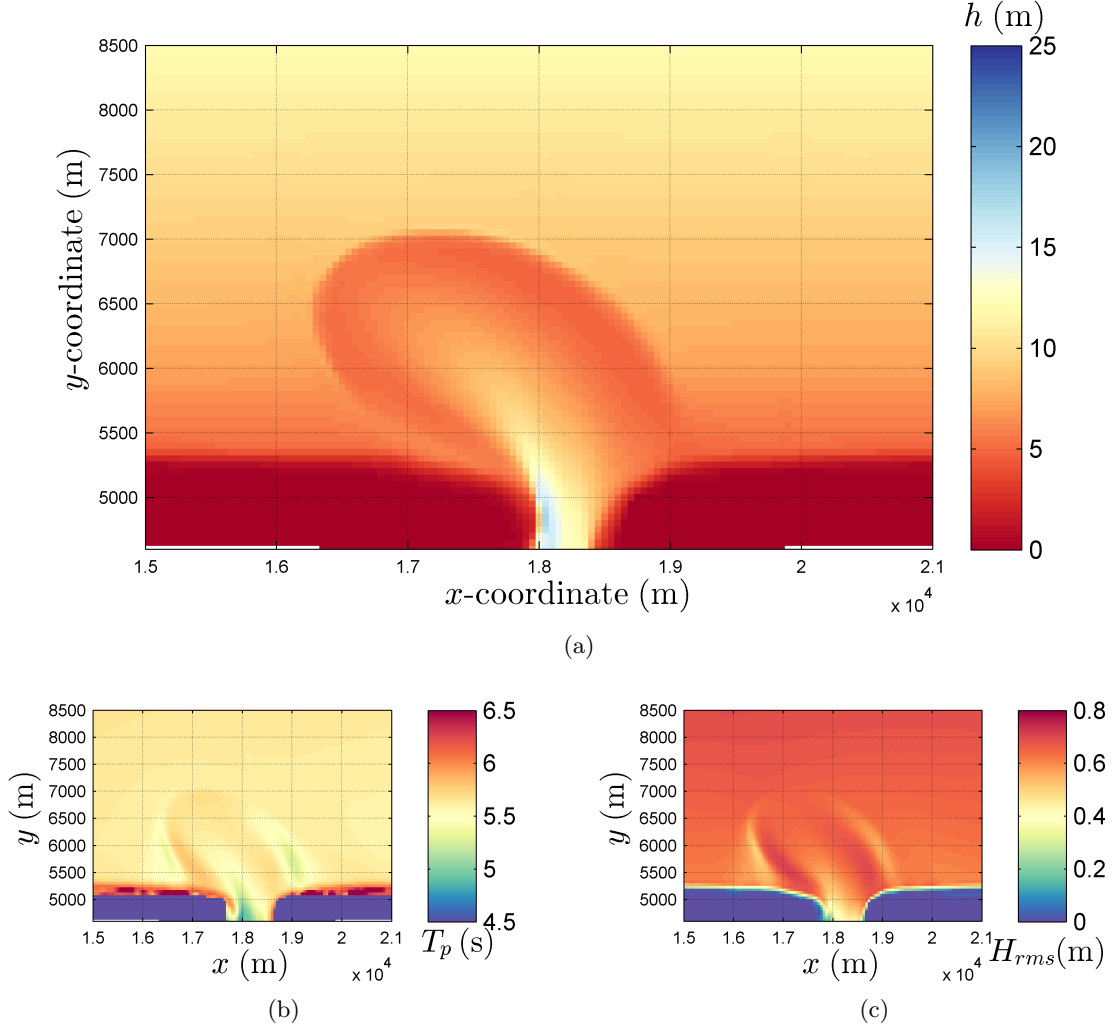
Figure 4.9: Panel (a) shows the water depth ($h = d + \eta$), panel (b) the peak period (T_p) and panel (c) the root-mean-square wave height (H_{rms}) for the idealised delta study when the along shore current has reach its maximum value to the east during a tidal cycle. The values are visualized after 4 years of modelling with the bulk method.

The values of H_{rms} show a higher value on the shoal but lower values on front of it. The increase in H_{rms} i.e. an increase in wave energy, arises due to refraction. The wave rays refract into the direction of the shoal. This lead to convergence of wave energy. Refraction also explains the lower values in front of the shoal similar as shown for the complex geometry study. Furthermore, the variations in H_{rms} are not shown when the wave reach the shoal perpendicular. In that case no refraction takes place. Similar to the behaviour of H_{rms}, the values for T_p are higher on the shoal.

Furthermore, in front of and in the channel T_p is lower.

Differences in u_b computed with the spectral method and the bulk method lead to differences in sand transport and morphology (see Figure 4.10). For the depths used in these simulations and based on the point model, the value of $u_{b,s}$ should be smaller than $u_{b,b}$ over the entire domain except in the deep area of the tidal inlet (see Figure 4.3). This last expectation is shown by the blue spot at $(1.8; 0.48) \cdot 10^4$ m in Figure 4.10(a). The ratio larger than 1 at the north and west side of the ebb-tidal delta results from the feedback between the morphology and the value of u_b. The increased ratio results from the different morphology used to calculate $u_{b,s}$ and $u_{b,b}$ in the last time step. The spectral method uses a smaller value of d and as a result a smaller value of h because the ebb-tidal delta extends further into the ocean. The enlargement of the ebb-tidal delta is the result of the lower value of u_b for the spectral method. This makes the system less wave dominant which results in an extension of the delta [*Bosboom and Stive*, 2015]. The volume of the ebb-tidal delta is also larger using the spectral method due to the reduction of wave influences.

Except an extension of the ebb-tidal delta into the ocean, the channel is also deepened. The increase in d is not in agreement with the point model. For the values of h in the channel, the spectral method should result in a lower value of u_b. Consequently, the equilibrium depth of the channel should decrease. On the other hand, the Delft3D simulations of the complex geometry showed a variation of the ratio between $u_{b,s}$ and $u_{b,b}$ during a tidal cycle. Although the ratio changed from larger than 1 to smaller than 1, the values in the channels were always higher than over the shoal. It is plausible that the value of $u_{b,s}$ averaged over a tidal cycle is higher than the value of $u_{b,b}$ in the channel and this would explain the deepening of the channel. This variation of the ratio in time is further discussed in Section 5.3.

Summary: The Delft3D simulation of the idealised delta formation resulted in a dynamically stable ebb-tidal delta. The simulations with the spectral method resulted in a delta which extended further into the ocean compared to a delta simulated using the bulk method. Furthermore, the depth of the channel was larger when the spectral method was used instate of the bulk method. The change in depth was not in agreement with the point model but this could be explained by considering the variations of the u_b ratio over time. This depth difference determined the ratio of u_b at the final time step.

The discussion of the results presented in this chapter is discussed in the next chapter. Chapter 5 will contain the comparison with literature, especially for the point model and the measurements. In addition, the Delft3D simulations showed an unexpected variation in the u_b ratio over time which should be further investigated. The research in this thesis should be related to the general applicability in hydrodynamic and morphological modelling. Finally, recommendations for further research will be provided in the next chapter.
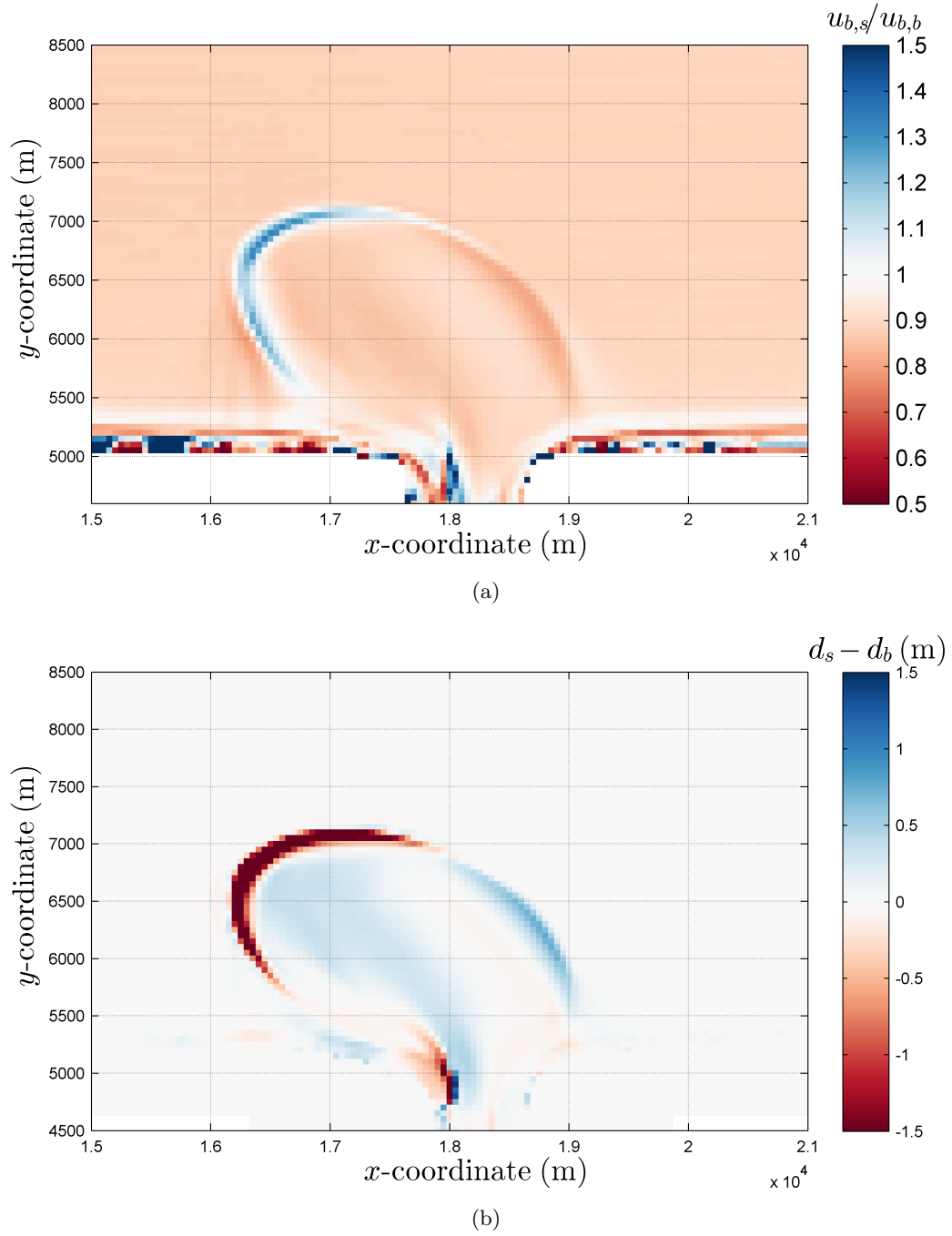
Figure 4.10: In panel (a) is shown the ratio of the bottom orbital velocity calculated by the spectral method ($u_{b,s}$) over the bottom orbital velocity calculated by the bulk method ($u_{b,b}$). In panel (b) the differences in bottom depth (d) is shown with d_s the bottom depth by the spectral method and d_b the bottom depth for the bulk method. Both panels visualize results after 4 years of modelling. The along shore current has reach its maximum value to the east during a tidal cycle.

Chapter 5
Discussion

The previous chapter presented and explained the results of the point model, measurements and two Delft3D simulations with regard to modelling of the bottom orbital velocity amplitude due to irregular waves. These results are further discussed in this chapter and a comparison with literature is made. Furthermore, several assumptions made in this study are verified. These subjects are discussed in the first four sections of this chaper, which are sorted similarly as in Chapter 4. The last section discusses the general applicability of this research and contains several recommendations for further research.

5.1 Point model

In addition to the three spectral shapes used by the point model (see Table 3.1), a fourth spectrum was investigated, namely that of monochromatic waves. For these waves the results of the spectral and bulk method should be identical. Due to the discretisation, the difference between both methods was 1.4%. The difference reduces when more bands are used because the minimum inequality between the peak frequency and the discretised frequencies of the spectrum is smaller. For 500 frequency bands, instead of 300, the difference between the bulk and spectral method for monochromatic waves was less than 1%.

The three spectra investigated by the point model are deep water wave spectra and this assumption should be considered. As a result, the spectra are only valid in deep water ($kh > \pi$, with k the wave number and h the depth). By the dispersion relation for deep water it can be written as

$$h > \frac{gT_p^2}{4\pi} \Rightarrow T_p < \sqrt{\frac{4\pi h}{g}} \tag{5.1}$$

with g as the gravitational acceleration [*Wiberg and Sherwood*, 2008]. The minimum value of h used in the point model is 5 m which results in $T_p < 2.51$ s. For $h = 10$ m it gives $T_p < 3.56$ s. Therefore, the point model uses spectra which are not valid for the lower values of h. The difference between the spectral method and the bulk method is relatively small for these values of h (see Figure 4.3). This emphasizes the importance of the spectral method, as the valid points show large differences and the situations where the spectra are not valid show small change. To investigate waves in shallow waters other types of spectra can be used, for example a TMA spectrum [*Bouws et al.*, 1985] or a FRF spectrum [*Miller and Vincent*, 1990].

The results of the point model are in good agreement with the results of *Soulsby* [1997] (see Figure 5.1). This was expected because both studies are based on the similar equivalent wave concept. Small difference arise related to the number of discretisation bands used in this study.
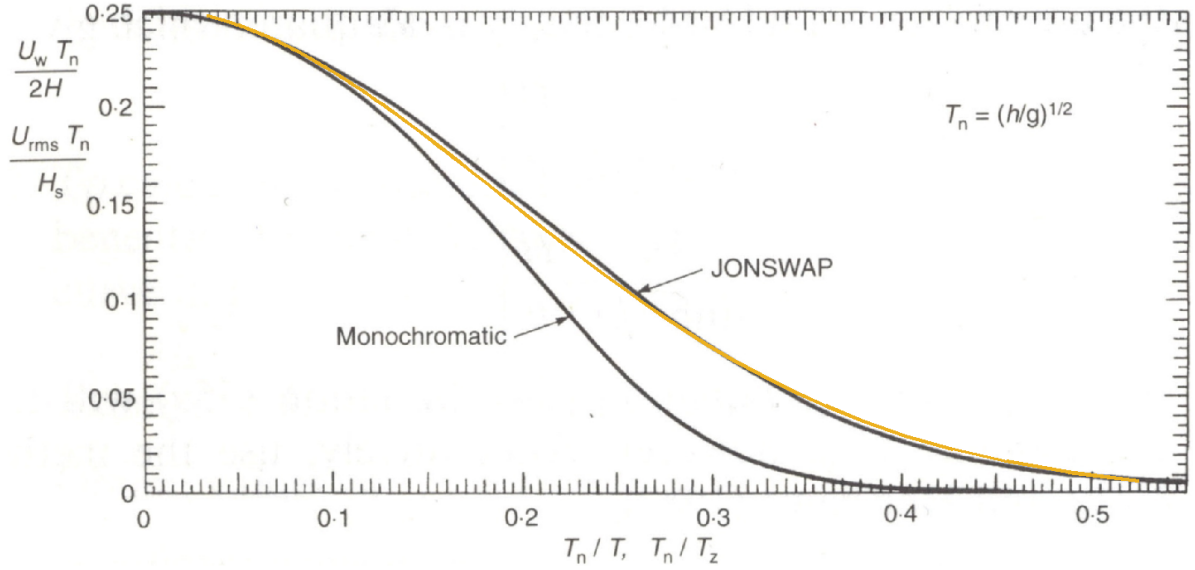
Figure 5.1: A reprint of [*Soulsby*, 1997] combined with the results of the point model, orange line. The figure shows the bottom velocity amplitude for monochromatic waves with U_w the bottom orbital velocity amplitude induced by a monochromatic wave, T_n a scaling period, H the wave height and T the period of the monochromatic wave. For irregulars waves u_{rms} indicates the root-mean-square bottom orbital velocity ($u_b = u_{rms}\sqrt{2}$ with u_b the bottom orbital velocity amplitude), H_s the significant wave height and T_z the zero upcrossing wave period. It is related to the peak period T_p by $T_z = 0.781T_p$ for a JONSWAP spectrum.

5.2   Verification with field data

The measured bottom orbital velocity ($u_{b,m}$) displays a cyclic behaviour with a period of 6 hours (see Figure 5.2). Several theories have been tested to explain this behaviour. First, the type of filtering was verified. The steep slopes in the frequency domain of the bandpass filter result in wiggles in the time domain [*Thomson and Emery*, 2014]. Instead of this ideal bandpass filter a Butterworth filter was used but the periodicity was not affected. Second, a redistribution of the velocity density over the different frequencies due to background velocity was verified. The spectra of the discrete velocity density ($E_{uv,i}$) changed with a period of 6 hrs, but the changes were not frequency dependent. The energy density over the entire spectrum increased and decreased with a period of 6 hrs. Therefore, the periodicity might result from turbulence due to the tidal velocity. This hypothesis is suggested because the time signal of the current velocity reveals a strong correlation with the periodicity of $u_{b,m}$ and a mechanism can be illustrated which explains the correlation. The energy of the large scale velocities is filtered out, but these velocities transport (turbulent kinetic) energy into smaller length scales by turbulent mixing. These smaller scales have partly the same frequency as u_b and influence the value of $u_{b,m}$. The velocity by these smaller scales is filtered out. An observation that supports this hypothesis was the change in $u_{b,m}$ when the cut of boundary was adjusted. The cut of boundary was reduced from 0.5 Hz to 0.3 Hz. In this range the wave induced velocity would be relative small compared to turbulent induced velocity. In line with the hypothesis, the reduction of $u_{b,m}$ was much smaller than the reduction of the amplitude of the periodicity. A decisive if the hypothesis is correct be found when a frequency-dependent filter based on the turbulent energy cascade [*Pope*, 2001] as done in *Zhu et al.* [2016].

The measurements of the surface elevation and bottom velocity are taken at two different locations (see Figure 3.1) and effects on the value of u_b due to this distance have been neglected. The difference in location results in different u_b values if the depth and/or the wave climate is
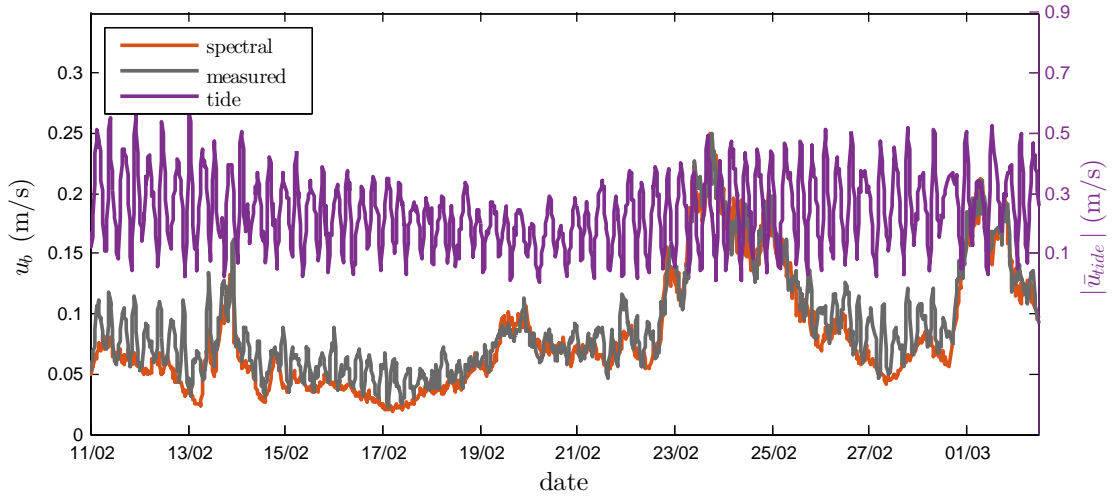
Figure 5.2: A time series of the bottom orbital velocity (u_b) based on measured 20 minutes segments of the bottom velocity. For the red line the value of u_b is calculated using the full wave spectrum ($u_{b,s}$) and the values of the grey line used the measured velocity signal ($u_{b,m}$) (see Figure 3.4(d)). The vertical axis at the right shows in purple the 20 minutes averaged magnitude of the measured velocity by the NEMO Lander. For clearness, continuous lines are shown although it are discrete measurements of 20 minutes.

different at the positions. Several reasons can be given why the discrepancy in location can be discarded. First, there is no significant difference between $u_{b,m}$ and $u_{b,s}$. Second, differences between $u_{b,m}$ and $u_{b,s}$ could arise due to difference in h of both sites. The difference in h between both sites is of similar magnitude as the tidal elevation. Consequently, if the difference in h between both location would be important then the value of $u_{b,s}$ should be influenced by the tidal elevation. The value of $u_{b,s}$ is not influenced by the tidal elevation (see Figure 3.4). Additionally, a difference in wave conditions exclusively occurs for southern wind due to the topography. In that case, the waves are very small due to the limited fetch length and the forces by waves on the bed be neglected.

As was mentioned in the Introduction, a comparison between the spectral method and the bulk method was already performed by *Wiberg and Sherwood* [2008], but in this study the measurements were performed in shallower water. The results of *Wiberg and Sherwood* [2008] are in line with the results found in this research: the value of $u_{b,s}$ had the best agreement with $u_{b,m}$, followed by the value of $u_{b,s}$ calculated with a JONSWAP spectrum. On the other hand, the discrepancies identified by *Wiberg and Sherwood* [2008] between the different methods for u_b were much larger than the inequalities found in this study.

5.3 Application complex geometry

As indicated in section 4.3, the ratio of $u_{b,s}$ over $u_{b,b}$ contains a variation during the tidal cycle (see Figure 4.7 and Figure 4.8). The ratio varies because the changes in $u_{b,s}$ are different from the changes in $u_{b,b}$ during a tidal cycle. The variation comes from the changes in depth and/or the current due to the tides. The periodicity is more likely due to the current than then depth, because the change in the depth offshore are relative small and the variations still prevail.

The periodic behaviour of $u_{b,s}/u_{b,b}$ is most likely due to the wave current interaction which results in a Doppler shift in the wave frequency. The variations in $u_{b,s}/u_{b,b}$ does not result from a change in the shape of the wave energy density spectrum. If that was the case the values of $u_{b,b}$ would not vary because they are independent of the shape.

For a sinusoidal wave in the presence of a current the dispersion relation reads

$$\sigma^2 = gk \tanh(kh) \tag{5.2}$$

with σ the relative angular frequency [*Holthuijsen*, 2007]. Physically, σ indicates the frequency of the wave with respect to moving frame of reference, for example the moving water. The frequency can also be defined in a fixed coordinate system, for example the bed. This absolute angular frequency is given by

$$\omega = \sigma + ku_n \tag{5.3}$$

with ω the absolute angular frequency and u_n the current velocity in the wave direction.

The variations of $u_{b,s}$ and $u_{b,b}$ were also studied individually and this showed that the variations of $u_{b,b}$ are much larger than the variations of $u_{b,s}$ within. An important piece of information in understanding the periodic behaviour of $u_{b,s}/u_{b,b}$ is knowing which wave frequency is used for $u_{b,s}$ and $u_{b,b}$. For $u_{b,s}$, σ is used whilst ω is input for $u_{b,b}$. Furthermore, the boundary conditions need to be considered because they are constant in time. The relative frequency, related to σ, is set as a boundary condition [*Smith*, 2016]. This could explain why the variations in $u_{b,b}$ are much larger than the variations in $u_{b,s}$ and could also explain the periodicity of $u_{b,s}/u_{b,b}$.

An order of magnitude analysis supports the hypothesis that the difference in type of frequency results in the periodic behaviour. Using the bulk method and $T = 4$ s, $g = 9.81$ m/s^2 and $h = 5$ m, the ratio of $u_{b,b}$ for $u_n = +0.5$ m/s over $u_{b,b}$ for $u_n = -0.5$ m/s is 1.56. This ratio increases for larger values of h and is of similar order of magnitude as the difference between the spectral method and the bulk method.

Due to the periodic behaviour of $u_{b,b}$ and the current, the residual sediment transport is effected. When the current is in the same direction as the waves the value of $u_{b,b}$ is smaller than the situation without a current. This increase results in a smaller sediment transport into the current direction. With an opposing current, the value of $u_{b,b}$ is larger and the sediment transport in the current direction is smaller. Averaged over a tidal cycle sediment is transported opposite to the wave direction by this mechanism. It should be considered that many more mechanisms influence the sediment transport, for example: wave asymmetry and tidal asymmetry.

5.4 Idealised delta formation

The simulations of the delta formation with idealised setting showed large variations at the dry/wet boundary (see Figure 4.9(a) and Figure 4.10(a)). These large variations are accepted, although they are not realistic because their influence on the ebb-tidal delta is limited. The variations could be reduced by applying a wet-dry diffusion coefficient [*Deltares*, 2015].

The settings and schematisation used in this study for the bulk method closely correspond with the research of *Ridderinkhof et al.* [2016b]. *Ridderinkhof et al.* [2016b] modelled the formation and migration of a sandy shoals on ebb-tidal deltas. The size and shape of the shoal simulated in this study is similar to the shoal modelled in *Ridderinkhof et al.* [2016b]. This was expected because the hydrological and morphological settings are almost identical.

5.5 Recommendations

5.5.1 Model specific

This study showed the effect of spectral wave properties on the value of u_b and several model specific recommendations are described in this section. First, the values of the empirical parameters

in Delft3D should be reconsidered when the spectral method is used. As was indicated in the Introduction, the modelling of sediment transport and the induced morphological changes is highly empirical. In this study the empirical parameters used in the bulk and spectral method are identical and changing these parameters will influence the value of $u_{b,s}$ and the changes in morphology.

Second, it would be interesting to further investigate the time variations of the ratio of $u_{b,s}/u_{b,b}$. It was hypothesised in Section 5.3 that the periodicity resulted from the difference in relative and absolute frequency. This hypothesis could be investigate by changing the Delft3D source code. The most straightforward method would be to convert the T_p, which is based on the absolute frequency, for the bulk method, to a T_p based on the relative frequency. A strong reduction of the amplitude of the periodic behaviour of $u_{b,s}/u_{b,b}$ would confirm the hypothesis.

The difference in the use of the absolute and relative frequency indicates a point of discussion related to the calculation of u_b: Which frequency should be used to calculate u_b? Based on linear wave theory, it can be argued that it should be the relative frequency. Linear wave theory is used to describe the transition from surface elevation to the velocity at the bottom. This transition happens through the water and because of that it can be argued that it should be dependent on the frequency through the water, the relative frequency. On the other hand, in this study the bulk and spectral method were compared with $u_{b,m}$. Here, the absolute frequency was used and no significant difference was found between the $u_{b,m}$ and $u_{b,s}$. This would suggest that the absolute frequency should be used.

Based on the results of the point model, the field data verification and the idealised delta formation other recommendations are suggested. One of them is that the point model can be upgraded to consider wave spectra that are valid in water of intermediate and/or small depth. Furthermore, the time series of $u_{b,m}$ shows an unexplained periodic behaviour. In Section 5.2, it was hypothesised that it was due to turbulent kinetic energy. A frequency-dependent filter is advised to verify this hypothesis. For the idealised delta study it is recommended to apply a the artificial shoal similarly as done by *Ridderinkhof et al.* [2016a]. Due to the artificial shoal the ebb-tidal delta starts to migrate. A point of interest would be the difference in migration speed of the ebb-tidal delta between the bulk and spectral method.

5.5.2 Applications

The relevance of this study is not limited to the modelling of ebb-tidal deltas. As was explained in the Introduction is an equivalent wave concept used to take into account the forces by waves on the bed for irregular waves in a phase averaged model. Consequently, the spectral method is applicable for the morphodynamic modelling of other bed forms when irregular waves are considered. Consequently, it is recommended to use the spectral method in other schematisations.

The importance and effects of implementing the spectral method is different for each situation. First, the spectral method becomes more important when the schematisation of the bathymetry contains large depth variations. The difference between the bulk and spectral method in the value of u_b is dependent on depth. When the depth changes over the domain a calibration procedure can not compensate for the difference. Second, the spectral method should be considered when the peak period is small ($\leq \sim 6$ s) or when the depths are large ($\geq \sim 10$ m). For these cases is the effect of the frequency-dependent reduction large. Also, when the wave spectrum contain two peaks, the width of the spectrum is large and/or the spectrum changes rapidly over the domain the spectral method should be considered.

When the spectral method is used, a reconsideration of the empirical parameter is advised. The values of the empirical parameters are based on the bulk method and are no longer valid when the spectral method is used. It is expected that noticeable difference still occur between the modelled

results of the spectral and bulk method. Differences should remain between both methods because the difference depends on location and moment of the tidal cycle.

The use of the spectral method is also advised because the computational effort of a simulation is barely influenced for Delft3D. Furthermore, the implementation of the spectral method is limited to adding a $\sqrt{(2)}$ in the source code (see Appendix B). The computational time is hardly influenced because the wave-module of Delft3D already determines a representative bottom orbital velocity and uses its value to determine the friction by the bottom. It can be shown that the value of this representative bottom orbital velocity can be written as $\sqrt{2}u_{b,s}$. The additional computational effort of the spectral method reduces to the communication of $u_{b,s}$ to the flow-module.

The default method in Delft3D to calculate u_b is slightly (a factor 1.12) different from the exact bulk method (see Appendix B). The factor 1.12 arises from considering the probability density function. When the spectral method is used the probability density function of the waves is already taken into account [*Holthuijsen*, 2007].

5.5.3   Further research

Topics of further research are related to the improved of the equivalent wave concept by integrating more spectral wave properties. Other, more advanced equivalent wave concepts exist and they could also be used. For example the formulation of *Madsen* [1994]. The formulation of *Madsen* [1994] is more advanced then *Soulsby and Smallman* [1986] because a weighted averaged period is defined instead of T_p, but the formulation is also more complicated. Both approaches use the same relation for $u_{b,s}$. Differences arise when the forces on the bed are studied because the period weakly effects the friction factor. The friction factor is used to translate the value of u_b to a bed shear stress.

The integration of other spectral wave properties can be challenging. Besides a wave energy spectrum, also a phase spectrum could be considered. Problems arise because in a phase averaged model the phase spectrum is not available. Furthermore, the interactions between waves with different frequencies are no longer zero when averaged over a wave period because the phase is no longer random.

Chapter 6
Conclusions

The aim of this study was to investigate spectral wave properties and its effects on bed level evolution induced by waves and current. Based on this aim three research question were defined:

1. How do the water depth, root-mean-square wave height, peak period and spectral shape influence the difference between a bottom orbital velocity amplitude calculated using the bulk method and the spectral method?
2. Is the calculated bottom orbital velocity amplitude significantly improved when a spectral method is used instead of a bulk method?
3. How does the spectral method used to compute the bottom orbital velocity amplitude and subsequent sediment transport influence the modelled morphodynamic behaviour of complex systems compared to the situation when the bulk method applied?

A point model, field measurements and two numerical models were used in this study. Each of the following sections is specifically linked to one of the research questions.

6.1 Point model

The difference between the bottom orbital velocity amplitude (u_b) calculated by the bulk and the spectral method was strongly dependent on the water depth and peak period (T_p). The value of u_b for the spectral method was between 20% lower and 60% higher relative to the value determined by the bulk method. A higher or lower value of u_b dependent on depth and T_p. The spectral method should be considered if T_p is small ($\leq \sim 6$ s) or the depth is large ($\geq \sim 10$ m).

The effects of the root-mean-square wave height and spectral shape on the difference between u_b calculated by the bulk and spectral method were limited. The root-mean-square wave height affected the absolute difference by both methods linearly, but it did not effect the ratio. The effect of the shape of the wave spectrum was linked to the width of it. When the shape of the spectrum was narrow, the difference between the bulk method and the spectral method was smaller compared to a wide spectrum.

6.2 Verification with field data

The comparison of the measured u_b with the u_b calculated from the surface elevation showed no significant difference when the spectral method was used. When the bulk method was used, a significant difference was found between the measured and calculated u_b. The root-mean-square difference between the measured and calculated u_b was reduced by 1/3 when the spectral method was used instead of the bulk method.

The spectral method was applied combined with a JONSWAP spectrum. The difference between this u_b value and the measured u_b was larger than for the full spectral method (the spectral method combined with the measured wave spectrum) but smaller than by the bulk method. The spectral method combined with a JONSWAP spectrum indicated that the reduction of the root-mean-square difference was related to the frequency-dependent reduction and the independency of T_p for the spectral method. Both effects were of equal importance.

6.3   Complex numerical modelling

The simulations of the ebb-tidal delta showed an increase of u_b in the deep channels and a decrease of the velocity over the shoals when the spectral method was used instead of the bulk method. When a higher value of T_p was used the relative difference between the bulk method and the spectral method was reduced. The value of u_b calculated by the spectral method varied over a tidal cycle.

For the spectral method, the modelling of the idealised ebb-tidal delta showed an increase in depth of the tidal channel. Furthermore, the depths used in these simulations resulted in a lower orbital velocity for the spectral method. This made the schematisations less wave dominant and resulted in a further extension of the ebb-tidal delta into the offshore direction. Also, the volume of the shoal increased.

Bibliography

Baher, H., *Analog and digital signal processing*, John Wiley & Sons, 2001.

Battjes, J. A., and J. P. F. M. Janssen, Energy loss and set-up due to breaking of random waves, *Coastal Engineering Proceedings*, *1*(16), 1978.

Bosboom, J., and M. J. Stive, *Coastal Dynamics I: Lecture Notes CT4305*, VSSD, 2015.

Bouws, E., H. Günther, W. Rosenthal, and C. Vincent, Similarity of the wind wave spectrum in finite depth water: 1. spectral form, *Journal of Geophysical Research: Oceans*, *90*(C1), 975–986, 1985.

Bretschneider, C. L., A one-dimensional gravity wave spectrum, *Ocean Wave Spectra*, pp. 41–56, 1963.

Chakrabarti, S. K., Unification of two-parameter energy spectrum models, *Journal of Waterway, Port, Coastal, and Ocean Engineering*, *112*(1), 173–176, 1986.

Colebrook, C. F., and C. M. White, Experiments with fluid friction in roughened pipes, *Proceedings of the royal society of london. series a, mathematical and Physical sciences*, pp. 367–381, 1937.

Crapper, G. D., *Introduction to water waves*, Ellis Horwood Ltd., 1985.

deltacommissaris, S., Deltaprogramma 2017: Werk aan de delta, 2016.

Deltares, D., Delft3d-flow user manual, *Delft, the Netherlands*, 2015.

EcoShape, Overview Building with Nature program, `http://www.ecoshape.nl/en_GB/overview-bwn.html`, 2016.

Eldeberky, Y., and J. A. Battjes, Spectral modeling of wave breaking: application to Boussinesq equations, *Journal of Geophysical Research: Oceans*, *101*(C1), 1253–1264, 1996.

Fredsøe, J., Turbulent boundary layer in wave-current motion, *Journal of Hydraulic Engineering*, *110*(8), 1103–1120, 1984.

Hasselmann, K., et al., Measurements of wind-wave growth and swell decay during the joint north sea wave project (JONSWAP), *Tech. rep.*, Deutches Hydrographisches Institut, 1973.

Herman, P. M. J., N. Villars, H. Winterwerp, T. van Kessel, Z. Wang, C. Briere, L. van Rijn, and J. Cleveringa, Analyse vaargeul Holwerd-Ameland, *Tech. rep.*, Deltares, 2016.

Hoefsloot, F., and K. Volleberg, Actualisatie en bouw baseline Zeeuwse Delta, rapportage CSO. Projectcode 13M2062. Versie 24 januari 2014, 2014.

Holthuijsen, L. H., *Waves in oceanic and coastal waters*, Cambridge University Press, 2007.

Jak, R. G., O. G. Bos, and H. J. Lindeboom, Instandhoudingsdoelen Natura 2000-gebieden Noordzee, *Tech. rep.*, IMARES, 2009.

Journée, J. M. J., and W. W. Massie, *Offshore hydromechanics*, TU Delft, 2000.

Komen, G. J., K. Hasselmann, and K. . Hasselmann, On the existence of a fully developed wind-sea spectrum, *Journal of physical oceanography*, *14*(8), 1271–1285, 1984.

Lesser, G. R., J. A. Roelvink, J. A. T. M. Van Kester, and G. S. Stelling, Development and validation of a three-dimensional morphological model, *Coastal engineering*, *51*(8), 883–915, 2004.

Longuet-Higgins, M. S., and R. W. Stewart, Radiation stress and mass transport in gravity waves, with application to surf beats, *Journal of Fluid Mechanics*, *13*(04), 481–504, 1962.

Madsen, O. S., Spectral wave-current bottom boundary layer flows, *Coastal engineering*, *94*, 384–397, 1994.

Manning, R., J. P. Griffith, T. F. Pigot, and L. F. Vernon-Harcourt, *On the flow of water in open channels and pipes*, 1890.

Mei, C. C., M. Stiassnie, and D. K. P. Yue, *Theory and applications of ocean surface waves: Linear Aspects*, World scientific, 2005.

Meirelles, S., M. Henriques, R. Horner-devine, Alexander, A. J. Souza, J. Pietrzak, and M. Stive, Bed shear stress on the middle shoreface of the South-Holland coast, in *The Proceedings of the Coastal Sediments 2015*, World Scientific, 2015.

Miller, H. C., and C. L. Vincent, FRF spectrum: TMA with kitaigorodskii's f-4 scaling, *Journal of Waterway, Port, Coastal, and Ocean Engineering*, *116*(1), 57–78, 1990.

Ockenden, M. C., and R. L. Soulsby, Sediment transport by currents plus irregular waves, 1994.

Pierson, W. J., and L. Moskowitz, A proposed spectral form for fully developed wind seas based on the similarity theory of SA Kitaigorodskii, *Journal of geophysical research*, *69*(24), 5181–5190, 1964.

Pope, S. B., *Turbulent flows*, IOP Publishing, 2001.

Ridderinkhof, W., Morphodynamics of ebb-tidal deltas, Ph.D. thesis, Utrecht University, 2016.

Ridderinkhof, W., P. Hoekstra, M. van der Vegt, and H. E. de Swart, Cyclic behavior of sandy shoals on the ebb-tidal deltas of the Wadden Sea, *Continental Shelf Research*, *115*, 14–26, 2016a.

Ridderinkhof, W., H. E. Swart, M. Vegt, and P. Hoekstra, Modeling the growth and migration of sandy shoals on ebb-tidal deltas, *Journal of Geophysical Research: Earth Surface*, *121*(7), 1351–1372, 2016b.

Sha, L. P., and J. H. Van den Berg, Variation in ebb-tidal delta geometry along the coast of the Netherlands and the German Bight, *Journal of Coastal Research*, pp. 730–746, 1993.

Shields, A., Anwendung der aehnlichkeitsmechanik und der turbulenzforschung auf die geschiebebewegung, *Tech. rep.*, Preussischen Versuchsanstalt für Wasserbau, 1936.

Smith, C., Delft3D implementation of SWAN: Spectral output in absolute frequency, boundries forced with intrinsic frequency, *Tech. rep.*, University of Miami, 2016.

Soulsby, R., *Dynamics of marine sands: A manual for practical applications*, Thomas Telford, 1997.

Soulsby, R. L., Calculating bottom orbital velocity beneath waves, *Coastal Engineering*, *11*(4), 371–380, 1987.

Soulsby, R. L., and J. V. Smallman, A direct method of calculating bottom orbital velocity under waves, 1986.

Soulsby, R. L., and R. J. S. Whitehouse, Threshold of sediment motion in coastal environments, in *Pacific Coasts and Ports' 97: Proceedings of the 13th Australasian Coastal and Ocean Engineering Conference and the 6th Australasian Port and Harbour Conference; Volume 1*, p. 145, Centre for Advanced Engineering, University of Canterbury, 1997.

Soulsby, R. L., L. Hamm, G. Klopman, D. Myrhaug, R. R. Simons, and G. P. Thomas, Wave-current interaction within and outside the bottom boundary layer, *Coastal engineering*, *21*(1-3), 41–69, 1993.

Thomson, R. E., and W. J. Emery, *Data analysis methods in physical oceanography*, Newnes, 2014.

Van Rijn, L. C., *Principles of sediment transport in rivers, estuaries and coastal seas*, vol. 1006, Aqua publications Amsterdam, 1993.

van Rijn, L. C., Unified view of sediment transport by currents and waves. i: Initiation of motion, bed roughness, and bed-load transport, *Journal of Hydraulic Engineering*, *133*(6), 649–667, 2007a.

van Rijn, L. C., Unified view of sediment transport by currents and waves. ii: Suspended transport, *Journal of Hydraulic Engineering*, *133*(6), 668–689, 2007b.

Vroom, J., P. L. M. de Vet, and J. J. van der Werf, Validatie waterbeweging Delft3DNeVla model Westerscheldemonding, *Tech. Rep. Version 4.0. WL Rapporten, 12_107*, Flanders Hydraulics Research & IMDC: Antwerp, Belgium, 2015.

Wiberg, P. L., and C. R. Sherwood, Calculating wave-generated bottom orbital velocities from surface-wave parameters, *Computers & Geosciences*, *34*(10), 1243–1262, 2008.

Yuan, J., Turbulent boundary layers under irregular waves and currents: Experiments and the equivalent-wave concept, *Journal of Geophysical Research: Oceans*, 2016.

Zhu, Q., B. C. van Prooijen, Z. B. Wang, Y. X. Ma, and S. L. Yang, Bed shear stress estimation on an open intertidal flat using in situ measurements, *Estuarine, Coastal and Shelf Science*, *182*, 190–201, 2016.

Zijl, F., M. Verlaan, and H. Gerritsen, Improved water-level forecasting for the Northwest European Shelf and North Sea through direct modelling of tide, surge and non-linear interaction, *Ocean Dynamics*, *63*(7), 823–847, 2013.

Zijlema, M., G. Stelling, and P. Smit, SWASH: An operational public domain code for simulating wave fields and rapidly varied flows in coastal waters, *Coastal Engineering*, *58*(10), 992–1012, 2011.

List of Figures

List of Tables

List of Symbols

Symbol	Units	Description
A	m	Tidal amplitude
$c_{g,x}$	m/s	Wave group velocity in x-direction
$c_{g,y}$	m/s	Wave group velocity in y-direction
c_θ	1/s	Wave velocity in θ-space
c_σ	s^2	Wave velocity in σ-space
d	m	Bottom depth
D	m	Sediment grain size
D_{50}	m	Representative sediment grain size
D_*	-	Dimensionless grain size
$\tilde{E}$	m^{2}s	Wave energy density
$\tilde{E}_i$	m^{2}s	Discrete wave energy density
f	1/s	Frequency
f	1/s	Coriolis parameter
f_i	1/s	Discrete frequency
f_L	1/s	Left cut-off frequency of wave spectrum
f_p	1/s	Peak frequency
f_R	1/s	Right cut-off frequency of wave spectrum
F_x	kg/(ms^2)	Wave induced force in x-direction
F_y	kg/(ms^2)	Wave induced force in y-direction
g	m/s^2	Gravitational acceleration
h	m	Local water depth
H_{rms}	m	Root-mean-square wave height
H_s	m	Significant wave height
k	1/m	Wave number
$\vec{k}$	1/m	Wave number vector
k_i	1/m	Discrete wave number
k_p	1/m	Peak wave number
m	-	Grid index in x-direction
M_{fac}	-	Morphological scaling factor
n	-	Grid index in y-direction
N	-	Number of frequency bands of the wave spectrum
$\tilde{N}$	m^{2}s^2	Wave action density
p	-	Soil porosity
S	m^3/s	Volume of transported sediment
S	m	Sources and sinks of wave action
$\overline{\overline{S}}$	kg/s^2	Radiation stress tensor
S_{xx}	kg/s^2	Diagonal element of radiation stress tensor
S_{xy}	kg/s^2	Non-diagonal element of radiation stress tensor
S_{yy}	kg/s^2	Diagonal element of radiation stress tensor
t	s	Time
T_p	s	Peak period of a wave spectrum
u	m/s	Current velocity in x-direction

|		
$\vec{u}$	m/s	Current velocity vector
u_b	m/s	Bottom orbital velocity
$\tilde{u}_{b,i}$	m/s$^{3/2}$	Discrete bottom orbital velocity density
$u_{b,s}$	m/s	Bottom orbital velocity amplitude calculated using spectral method
v	m/s	Current velocity in y-direction
x	m	Horizontal dimension in longitudinal direction
y	m	Horizontal dimension in latitudinal direction
γ	-	Shape parameter of wave spectrum
Δf	1/s	Width of a frequency band
Δt	s	Time step
$\Delta \phi$	-	Tidal phase difference along boundary
η	m	Sea surface elevation
θ_{cr}	-	Critical shields parameter
θ_p	-	Dominant incoming wave direction at simulation boundary
ν	m^2/s	Kinematic viscosity of water
ν_e	m^2/s	Horizontal eddy viscosity
ξ	-	Shape parameter of wave spectrum
ρ	kg/m^3	Density of water
ρ_s	kg/m^3	Density of the sediment grains
σ	1/s	Relative frequency
τ_{cr}	kg/(ms^2)	Critical bed shear stress
τ_x	kg/(ms^2)	Combined wave and current induced bed shear stress in x-direction
τ_y	kg/(ms^2)	Combined wave and current induced bed shear stress in y-direction
ϕ_b	-	Angle of incoming wave with respect to the cross-shore direction at breaking
χ	-	Shape parameter of wave spectrum
ω	1/s	Angular frequency
ω_i	1/s	Discrete angular frequency
ω_{M2}	1/s	Angular frequency of semidiurnal tide
ω_p	1/s	Peak angular frequency

Appendix A
Additional figures
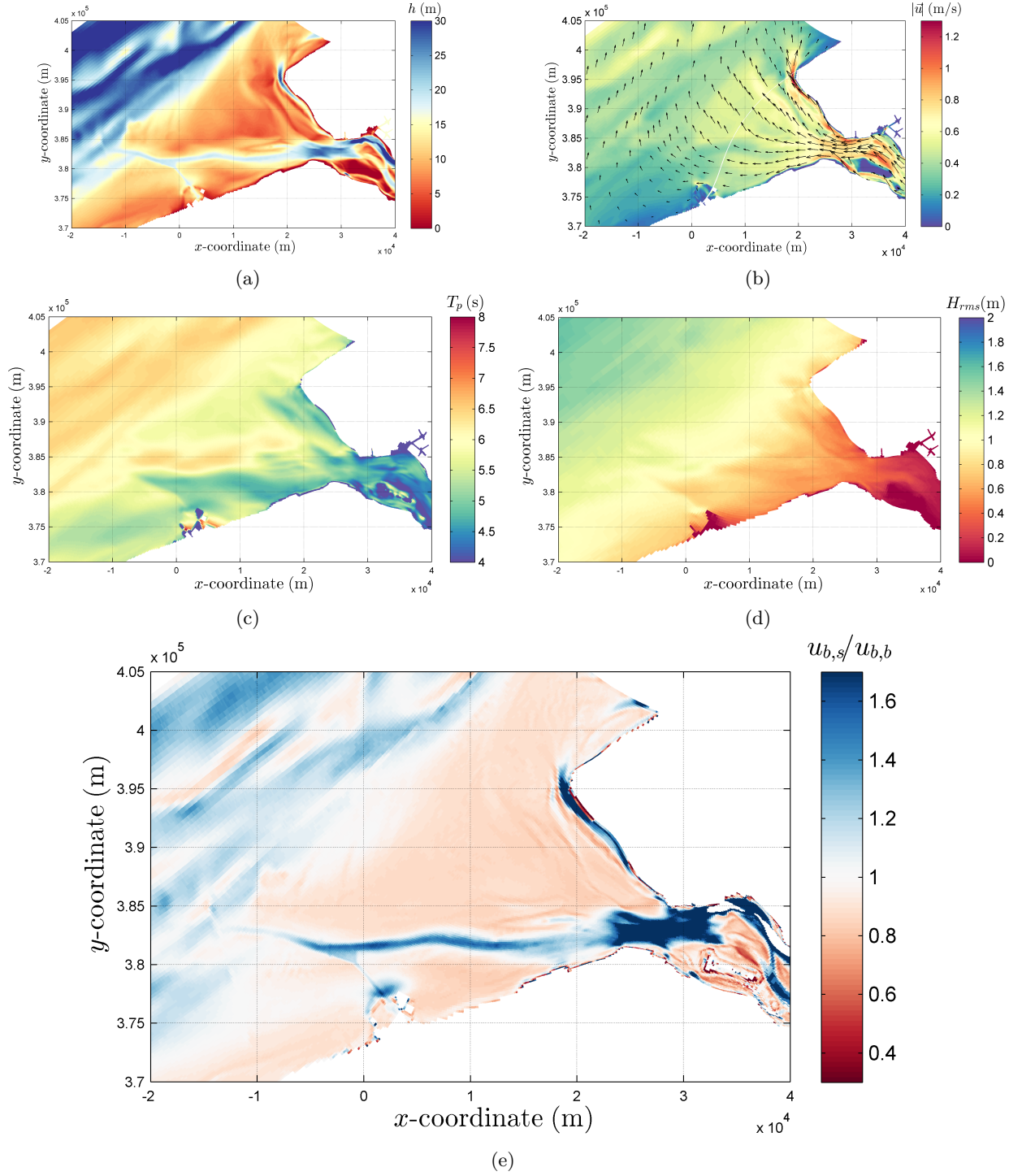
Figure A.1: The modelled hydrodynamics for the complex geometry 20 hours after spin-up ($t = 20$ hrs) for storm conditions (see Table 3.3). Panel (a) shows the water depth (h). In panel (b) the colour indicates the magnitude of the velocity ($|\vec{u}|$), the arrows are aligned with the local velocity direction and scale with the magnitude of the velocity. The white line crossing the domain indicates the boundary between two grids. The peak period (T_p) is shown in panel (c) and panel (d) displays the root mean square wave height (H_{rms}). Panel (e) presents the ratio between the bottom orbital velocity calculated by the spectral method ($u_{b,s}$) and determined by the bulk method ($u_{b,b}$).

Appendix B
Changes Delft3D source code

The default version of Delft3D (flow version 6.02.07.6118) uses a slightly different formulation to calculate the bottom orbital velocity amplitude then the bulk method. This Appendix gives an overview of the different formulations, explains the implementation of the current formulation and describes how easy the spectral method can be implemented in Delft3D.

The three different formulations to calculate the bottom orbital velocity amplitude are:

$$u_{b,b} = \frac{\pi f_p H_{rms}}{\sinh(kh)} \tag{B.1}$$

$$u_{b,s} = \pi \left[\int_0^\infty \frac{8 f^2 E}{\sinh^2(kh)} df \right]^{\frac{1}{2}} \tag{B.2}$$

$$u_{b,D3D} = \frac{\sqrt{\pi}}{2} \cdot \frac{\pi f_p H_{rms}}{\sinh(kh)} \tag{B.3}$$

with $u_{b,b}$, $u_{b,s}$ the bottom orbital velocity amplitude for the bulk and spectral method, $u_{b,D3D}$ the bottom orbital velocity amplitude calculated in Delft3D, f_p indicates the peak wave frequency, H_{rms} the root mean square wave height, k the wave number, h water depth and f the wave frequency. The formulation of the bulk method is such that for a narrow wave spectrum the values of $u_{b,b}$ and $u_{b,s}$ are the same. The formulation used in Delft3D follows from assuming a narrow spectrum and integrating this spectrum over the probability density function. In this derivation, the probability density function is assumed to be Rayleigh distributed (see Box B)

The changes in the source code and computational time are small when the spectral method is used instead of the bulk method. As was stated in the Discussion, the computational time is hardly influenced because the wave-module of Delft3D already determines a representative bottom orbital velocity and uses this value to determine the friction by the bottom. Delft3D already stores this value in its communication file. The settings of Delft3D-flow need to be such that it reads this value from the communication file. This is done by placing "ubcom = #Y#" in the mdf file. In the source code a $\sqrt{2}$ needs to be added to compensate for the difference in definition of u_b. The value from the communication files is a factor $\sqrt{2}$ too large. Consequently, the imported u_b needs to be devided by $\sqrt{2}$. Importing the value of u_b happens in the setwav.f90 file.

Box B

For a sinusoidal wave with frequency f_p the value of u_b is given by:

$$u_b = \frac{\pi f_p H}{\sinh(kh)}$$

with H the wave height. The value of H is defined by a probability density function. Integration over this function results in the averaged value of u_b and can be written as

$$\langle u_b \rangle = \int_0^\infty \frac{\pi f_p H}{\sinh(kh)} P(H) dH$$

---

with $\langle\rangle$ indicating the averaged value and $P(H)$ indicating the chance on wave height H. When the value of $P(H)$ is described by a Rayleigh distribution it can be written and simplified to

$$\langle u_b \rangle = \frac{\pi f_p}{\sinh(kh)} \int_0^\infty H \frac{2H}{H_{rms}} e^{-\left(\frac{H}{H_{rms}}\right)^2} dH = \frac{\pi f_p}{\sinh(kh)} \frac{H_{rms}\sqrt{\pi}}{2} = \frac{\sqrt{\pi}}{2} \cdot \frac{\pi f_p H_{rms}}{\sinh(kh)}$$